POLITECNICO
MILANO 1863

SCUOLA DI INGEGNERIA INDUSTRIALE
E DELL'INFORMAZIONE

# Ultrafast spectroscopy for semiconductor metasurfaces

**Tesi di Laurea Magistrale in**
**Engineering Physics - Ingegneria Fisica**

Author: **Andres Valladares y Tacchi**

Student ID: 953529
Advisor: Prof. Giulio Cerullo
Co-advisors: Mert Akturk
Academic Year: 2022-23

# Contents

# List of Figures

# Abstract

Sub-picosecond polarization control is an essential functionality in many applications, from encoding information to probing complex systems such as chiral molecules. In this context, metasurfaces have emerged as a promising solution for the development of polarization-sensitive compact devices reconfigurable in ultrashort timescales via interaction with intense femtosecond laser pulses. In this work, we performed two different pump-probe experiments aimed at characterizing the transient anisotropic features of an AlGaAs nanowire metasurface. Our results show that this design is capable of giant modulations of dichroism, up to 470% for TM polarized light, and birefringence, exhibiting wave-plate like functionalities with relative phase modulations up to $\pi/2$. This response is enabled by an extended state resonance tunable by all-optical means near the bandgap of the semiconductor where the band-filling effect dominates.

# Sommario

Il controllo della polarizzazione su scala temporale inferiore al picosecondo è una funzionalità essenziale in molte applicazioni, dalla codifica delle informazioni allo studio di sistemi complessi come le molecole chirali. In questo contesto, le metasuperfici sono emerse come una soluzione promettente per lo sviluppo di dispositivi compatti sensibili alla polarizzazione e riconfigurabili in tempi ultrabrevi tramite l'interazione con intensi impulsi laser a femtosecondi. In questo lavoro abbiamo eseguito due diversi esperimenti pump-probe volti a caratterizzare le proprietà anisotrope transitorie di una metasuperficie composta da nanofili di AlGaAs. I nostri risultati mostrano che questa configurazione è capace di enormi modulazioni del dicroismo, fino a 470% per stati di polarizzazione TM, e della birifrangenza, mostrando funzionalità simili a un ritardatore con modulazioni di fase relativa fino a $\pi/2$. Questa risposta è dovuta alla presenza di una risonanza associata ad uno stato esteso riconfigurabile unicamente per via ottica e posizionata vicino al band-gap del semiconduttore dove domina l'effetto di band-filling.

# Chapter 1

# Introduction

Polarization, i.e. the oscillation direction of the electric field of an electromagnetic wave, is one of the intrinsic properties of light and thus represents a fundamental aspect of understanding a huge variety of natural phenomena involving light-matter interaction. Therefore, the ability to detect and manipulate the state of polarization is of crucial importance in many fields of research and technological applications. In particular, since polarization is uncorrelated with the other degrees of freedom of light (amplitude, phase and frequency), it can be exploited as an additional information channel for telecommunications. Indeed, active control of polarization is already been extensively used as an encoding technology in optical links where switchable polarization-sensitive elements are reconfigured via electro-optical or magneto-optical effects. However, control of polarization in conventional optics relies on propagation through thick bulk media, precluding the development of miniaturized devices suitable for nanophotonic applications. Moreover, active reconfiguration based on electric actuators is fundamentally limited to gigahertz switching speeds.
To overcome these issues, bidimensional arrays of resonant nanostructures, known as metasurfaces, have been proposed as efficient and compact devices for ultrafast polarization switching on a subwavelength

scale. In these devices, the optical response can be engineered at will by a proper arrangement of highly polarizable nanoparticles. Specifically, giant anisotropic features can be synthetized with suitable inclusions resulting in remarkable dichroic responses and huge birefringence. Furthermore, these nanoparticles are characterized by a series of ultrafast relaxation processes, taking place in a sub-picosecond timescale after optical pumping, which are inherently linked with variations of the optical properties via non-equilibrium carrier distributions. Therefore, active reconfiguration can be achieved through an all-optical scheme in which an external optical stimulus is used to transiently modify the optical response, enabling terahertz modulation speeds.

The ability to access such short time scales has been made possible only by advances in ultrafast spectroscopy, a series of experimental techniques aimed at studying photoinduced dynamical processes providing high temporal resolution by exploiting ultrashort laser pulses. Indeed, both the control and the characterization of ultrafast processes can only be achieved by probing the system with pulses much shorter than its temporal evolution. The simplest of these techniques is called pump-probe spectroscopy: an intense laser pulse (pump), used to excite the sample via linear absorption, is followed by a second weaker pulse (probe) that monitors the pump-induced transient response at different time delays with respect to the pump arrival. The temporal evolution of the system can be then retrieved by recording the probe spectrum as a function of the time delay between pulses.

Here we present a reflective anisotropic metasurface based on AlGaAs nanowires for polarization control. A customized pump-probe setup was used to perform two different experiments aimed at characterizing the sample transient dichroism and birefringence.
The thesis is organized as follows:

- **Chapter 2** provides an overview of the main relevant concepts needed to understand how light manipulation can be achieved with metasurfaces. Section 1 highlights the importance of artificial periodic media in the control of optical beams, comparing photonic crystals and metamaterials. Section 2 focuses on resonant nanoparticles, the constitutive blocks of metamaterials, describing their optical properties and discussing the different materials employed in their realization. Section 3 explains how these blocks can be exploited in the realization of metasurfaces describing characterization methods, reconfiguration techniques and applications.

- **Chapter 3** reviews the main topics required to understand the results of the experiments here presented, as well as the setup employed. Section 1 discusses pulse propagation in nonlinear media. Sections 2 to 5 summarize the main second and third order nonlinear effects exploited in our setup. Section 6 explains how to perform and interpret a pump-probe measurement, describing the different physical mechanisms involved.

- **Chapter 4** discusses in detail the sample and the setup used for the characterization of its anisotropic properties. Section 1 focuses on the sample description and fabrication process. Section 2 discusses the technique used for polarization reconstruction in one of the experiments while section 3 provides a complete description of the pump-probe setup.

- **Chapter 5** presents the results of our measurements, comparing them to the simulated values and providing an explanation of the observed behavior.
- **Chapter 6** summarizes the conclusions that can be drawn from the results obtained.

# Chapter 2

# Introduction to metasurfaces

The increasing demand for higher data storage capacity and faster information transfer and processing has been met with many efforts in replacing currently available electronic technologies, which are quickly reaching their limits in terms of speed and miniaturization, with better performing optical devices. However, the control of light in conventional optical systems relies on propagation through optically thick media resulting in low efficiency bulk configurations and thus precluding the development of photonic integrated devices. Moreover, the limited capabilities of manipulating electromagnetic waves offered by natural materials restrict the number of implementable functionalities. To face these issues, great interest has been devoted to the realization of artificial materials with unique optical properties. In this context, planar composites of nanostructured scatterers, known as metasurfaces, represent the most promising solution due to their ability to alter the properties of light on a sub-wavelength scale.
This chapter is structured as follows: first we discuss the importance of periodic media in optics, presenting the most important milestones in the realization of artificial media by introducing photonic crystals and

metamaterials. Then we focus on resonant nanoparticles, the constitutive blocks of metamaterials, explaining their properties and comparing the most employed materials in their realization. Finally, we discuss how these can be exploited in the development of metasurfaces, the 2D counterpart of metamaterials.

## 2.1 Optics of periodic media

Structures exhibiting a periodic spatial variation of one or more of their defining quantities are fundamental elements in the development of technologies for the control of optical beams, offering the capability to tailor selective behavior in frequency, direction of propagation and polarization. Homogeneous materials like crystals do not allow for complete manipulation of light since their optical properties are given by the particular arrangement of their atoms, which cannot be engineered at will. For this reason, periodic inhomogeneities have been at the center of intensive research since the $18^{\text{th}}$ century with the discovery of diffraction gratings, consisting in a periodic modulation of the interface between two or more media on the wavelength scale. The interference between waves due to the periodicity of these structures gives rise to a frequency dependent transmitted (or reflected) angle of the incident light which can be exploited in many applications including monochromators, spectrometers, flat lenses and frequency multiplexing devices. As it is well known, this frequency selective behavior is also encountered in homogeneous dispersive materials, such as prisms, in which wavelength separation is caused by the frequency dependent nature of the refractive index. However, the increasing demand for miniaturization of optical devices makes them not suitable for the manipulation of electromagnetic waves in nanophotonic applications. Furthermore, the need for more complex structuring and localization of light on the sub-wavelength scale has forced scientists to look beyond

these simpler devices resulting in the development of artificial materials with unusual optical properties that cannot be obtained with ordinary media. The first class of these materials to be investigated were the Photonic Crystals (PCs) consisting in a periodic arrangement of high and low dielectric constant unit cells in at least one dimension, leading to multiple reflected waves that, interfering with one another, give rise to frequency ranges for which light cannot propagate, namely the photonic bandgaps. The interest in PCs arose from the pioneering work of Yablonovich (1987) [1], who demonstrated that photonic bandgaps allow for the inhibition of spontaneous emission and strong field localization. A decade later another class of artificial materials based on sub-wavelength resonant scatterers, which are now referred to as metamaterials (MMs), gained popularity thanks to Pendry's work on negative refractive index media (2000)[2].

Even though both classes of materials rely on resonant behavior, the physical mechanisms involved are quite different. Resonances in MMs are due to the high polarizabilities of their constitutive blocks, achievable by employing either plasmonic materials or high refractive index dielectrics, and are mostly concentrated in the region of the single unit cell. In PCs instead, they arise from diffraction effects which give rise to constructive and destructive interferences between scattered waves. In order to have diffraction, the distance between unit cells should be of the order of the wavelength for which the bandgap is needed, while in MMs the lattice constant is typically much smaller than the wavelength. As a consequence, for MMs, it is possible to define effective parameters, such as effective magnetic permeability $\mu$ and effective electric permittivity $\varepsilon$.

Despite the initial interest in 3D MMs, the attention gradually shifted toward the 2D version, now called metasurfaces (MSs), due to easier and less expensive fabrication processes, smaller sizes and lower losses.

## Photonic crystals (PCs)

PCs are structures exhibiting a periodic modulation of their dielectric function, obtained by alternatively stacking different materials in one or more directions (see fig. 2.1a). The geometric arrangement of these materials can be described by a Bravais lattice, defined by a set of non coplanar primitive vectors $(\mathbf{a}_1, \mathbf{a}_2, \mathbf{a}_3)$, such that $\mathbf{R} = n\mathbf{a}_1 + m\mathbf{a}_2 + l\mathbf{a}_3$ identifies the position of each point of the lattice. Given these points, it is possible to fill the whole space by translating a suitable geometric figure, called primitive unit cell, through all the points of the lattice. An important case is the Wigner-Seitz primitive cell, defined as the region of space closest to a certain lattice point than any other and having the property of sharing the symmetry of its lattice. The physical properties of the system are defined by assigning at each point a so called *basis* given by the permittivity tensor $\varepsilon(\mathbf{r})$, which repeats itself in space with period $\mathbf{R}$. Since $\varepsilon(\mathbf{r})$ is periodic in space it can be expanded in Fourier series resulting in a discrete set of spatial frequencies described by the vector space $\mathbf{G} = n\mathbf{b}_1 + m\mathbf{b}_2 + l\mathbf{b}_3$. It can be shown that the set of points identified by $\mathbf{G}$ has the properties of a Bravais lattice and admits a Wigner-Seitz cell, called the First Brillouin Zone (FBZ). The FBZ provides a complete description of the optical properties of a PC since the wave vector $\mathbf{k}$ of any mode propagating inside the PC must belong to it. These considerations highlight the importance of symmetry as a powerful tool to get insight into the eigenmodes of PCs without recurring to cumbersome calculations based on Maxwell's equations, summarized by the Bloch Electromagnetic Theorem. This theorem states that in a PC with primitive vectors $\mathbf{a}_i$ $(i = 1, 2, 3)$, the harmonic modes can be factorized into a periodic envelope and a plane wave term as follows:

$$\mathbf{E}(\mathbf{r}) = \mathbf{E}_{\mathbf{k},n}(\mathbf{r}) = \mathbf{u}_{\mathbf{k},n}(\mathbf{r})e^{i\mathbf{k}\cdot\mathbf{r}} \qquad \mathbf{u}_{\mathbf{k},n}(\mathbf{r}+\mathbf{a}_i) = \mathbf{u}_{\mathbf{k},n}(\mathbf{r}) \qquad (2.1a)$$

$$\mathbf{H}(\mathbf{r}) = \mathbf{H}_{\mathbf{k},n}(\mathbf{r}) = \mathbf{v}_{\mathbf{k},n}(\mathbf{r})e^{i\mathbf{k}\cdot\mathbf{r}} \qquad \mathbf{v}_{\mathbf{k},n}(\mathbf{r}+\mathbf{a}_i) = \mathbf{v}_{\mathbf{k},n}(\mathbf{r}) \qquad (2.1b)$$

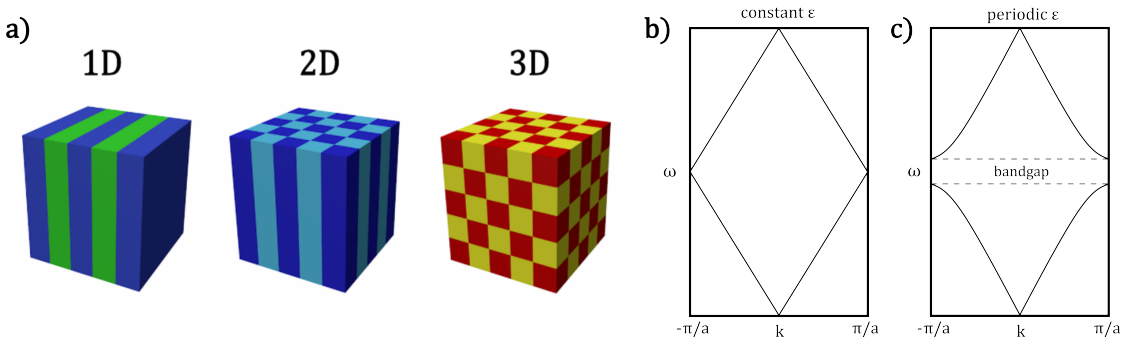


**Figure 2.1:** (a) 1D, 2D and 3D PCs, different colours indicate different values of permittivity. (b) Dispersion relation of a homogeneous medium with artificial periodicity $a$. (c) Dispersion relation of a medium with real periodicity $a$ exhibiting the presence of a bandgap.

The Bloch theorem results in a set of independent modes with wave vector $\mathbf{k}$, corresponding to solutions with different frequency $\omega$. Any value of $\mathbf{k}$ displaced by $\mathbf{G}$ will result in the same solution so it is possible to restrict calculations to the FBZ without loss of generality. For any given value of $\mathbf{k}$ in the FBZ there are countably many solutions indexed by $n$, called band index. The most important consequence of the Bloch theorem is that it describes the existence of dispersion relations $\omega = \omega_n(\mathbf{k})$, describing the band structure of the PC. Calculation of the dispersion relations reveals the presence of bandgaps, i.e. frequency ranges where no propagating modes exist. The origin of these bandgaps can be explained simply with the following qualitative arguments. We start considering a 1D homogeneous medium in which harmonic modes are left and right propagating plane waves having linear dispersion relation. We introduce an artificial periodicity by dividing the medium in slices of thickness a. The periodicity will result in a folding of the band structure at the edge of the FBZ, as shown in figure 2.1b, creating a degeneracy between the two modes. We now introduce a real weak periodicity which, acting as a perturbation, will break the degeneracy splitting the two modes and thus

opening a bandgap (fig. 2.1c). This is equivalent to what happens in quantum mechanics when two degenerate bare states are split into different dressed states by an external perturbation. The photonic bandgap represents the main aspect of the technological applications of PCs and can be exploited to realize filters, omnidirectional mirrors, nanoscale resonators and waveguides.

## Metamaterials (MMs)

A MM is an artificial structure composed of an array, usually periodic, of nano-sized scatterers that behave as artificial atoms, thus called meta-atoms. By properly engineering size, shape, orientation and arrangement of these constitutive blocks, one can obtain electromagnetic properties that are not observed naturally, and with the advantage of having more tunable degrees of freedom compared to PC configurations.

In the last 20 years, a particular interest has been devoted to MMs with simultaneously negative values of permittivity ($\varepsilon$) and permeability ($\mu$), called Double Negative materials (DNG). This work was first initiated by Veselago who demonstrated in a paper published in 1968 [3] that such a choice of these parameters leads to electrodynamic properties that can be described by a negative index of refraction. The main consequence is that waves propagating inside of DNG media have antiparallel Poynting vector $\mathbf{S}$ and wavevector $\mathbf{k}$, resulting in many exotic phenomena such as negative refraction at the interface between positive and negative index material, i.e. light is refracted on the same side of incidence with respect to the normal direction.

Despite these outstanding results, Veselago's discoveries remained in the background for many years due to the absence of DNG media in nature. Even though the idea of realizing artificial materials as a way to engineer unusual properties was already known back then, their development was hindered by the limited fabrication techniques available

at the time.
Moreover, one of the main challenges to this day has been to find an efficient way to characterize the optical response of MMs such that complex designs and functionalities can be engineered in a straightforward and intuitive manner. One way to tackle this problem is suggested by the electromagnetic models used to describe naturally occurring materials. The optical properties of conventional materials are defined by the motion of electrons under the influence of electric and magnetic forces applied by an electromagnetic wave. This collective response can be summarized by two fundamental parameters, permittivity and permeability, which provide a macroscopic representation of the underlying microscopic phenomenon.
Similarly, when dealing with nanostructured artificial materials, one would like to retrieve effective parameters for the characterization of the structure's behavior as a whole, enabling the use of Maxwell's equation to study its interaction with light. Such a procedure, called homogenization, was first proposed by John Pendry in a paper published in 1999 [4] and consists in defining a set of macroscopic fields by averaging the local fields over a certain volume of the unit cell. This method can be applied as long as the distance between unit cells is much smaller than the wavelength of the incident light, which is exactly the same criterion that allows to consider standard media as homogeneous.
In the same paper, Pendry used the homogenization procedure to retrieve the effective permeability of a 2D array of infinitely long conductive cylinders showing that a weak anisotropic diamagnetic response, tunable by geometric means, could be engineered starting from non-magnetic materials. This artificial magnetic behavior is due to circulating currents in the cylinders excited by an external field. He further showed that this response could be enhanced by employing a structure made of two concentric cylinders in a split-ring configuration, shown in

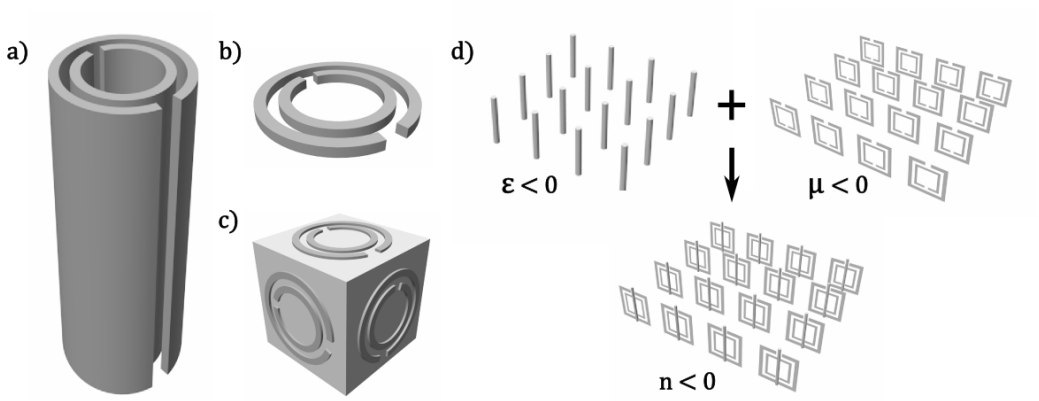


**Figure 2.2:** (a) Split-ring cylinder. (b) Split Ring Resonator (SRR). (c) Isotropic configuration of SRR. (d) Negative index material

figure 2.2a. The presence of the gap prevents the current from flowing around the rings but the capacitance between them still allows the current to flow. The introduced capacitance leads to a resonant behavior of the effective permittivity which exhibits negative values for certain ranges of frequency.
Furthermore, an isotropic response can be obtained by replacing the cylinders with flat disks, known as Split Ring Resonators (SRR) (fig. 2.2b), and arranging them to create a cubic lattice structure (fig. 2.2c). Shortly after, by combining these results with those previously obtained regarding a 2D array of thin conductive wires exhibiting negative values of the permittivity [5], it was possible to obtain a material having a negative refractive index in the microwave domain (fig. 2.2d).

## 2.2 Resonant nanoparticles

In recent years particles of sizes between 1 and 100 nm, called nanoparticles (NPs), have attracted the attention of scientists in many fields of research due to their unique scattering properties which allow localiza-

tion and manipulation of light on the sub-wavelength scale. The optical response of these structures shows a strong resonantly enhanced polarization highly dependent on their size, shape and surrounding medium, making them ideal constitutive building blocks in the realization of artificial materials with desired optical properties. The first NPs exploited plasmonic resonances in noble metals. These structures show a strong electric dipolar character due to the excitation of Localized Surface Plasmon (LSP), a non-propagating collective oscillation of the conduction electrons in the metal coupled to the electromagnetic field [6]. However, the metallic nature of these materials presents several drawbacks due to ohmic losses and thermal dissipation [7]. Furthermore, their optical response, dominated by resonances of electric dipolar type, limits the ability to engineer the directionality of the scattered light [8]. These issues represent a constraint in improving the performance of plasmonic material-based devices, creating the demand for an alternative route to achieve nanoscale control of light. More recently high-index dielectric and semiconductor NPs, which exploit Mie-resonances instead of plasmonics, have been proposed to achieve both electric and magnetic resonances of comparable strength with very low losses. The low dissipative nature of Mie-resonant NPs is ascribable to the excitation of displacement currents which, in the spectral region far from their main absorption band, largely exceed the conduction ones responsible for ohmic losses [9]. Furthermore, these materials allow for the development of devices compatible with CMOS fabrication processes [10]. Due to these unique advantages, high-index dielectric NPs are quickly replacing plasmonic materials in the realization of metadevices.

In this section, we review the main aspects of the resonant behavior of NPs. To simplify the discussion we only consider the case of a homogeneous isotropic sphere of radius $R$ having refracting index $n$, embedded in an isotropic and non-absorbing medium with refracting index $n_m$.

The scattering from a spherical particle of arbitrary size subjected to a plane wave can be rigorously described by Mie theory [11], which consists of a full vectorial treatment of Maxwell's equations in spherical coordinates. The Mie solution is given by an infinite series of multipoles characterized by the electric and magnetic Mie coefficients $a_n$ and $b_n$, which represent the amplitudes of the scattered fields by the sphere upon illumination:

$$a_n = \frac{m\Psi_n(mx)\Psi'_n(x) - \Psi_n(x)\Psi'_n(mx)}{m\Psi_n(mx)\xi'_n(x) - \xi(x)\Psi'_n(mx)} \tag{2.2a}$$

$$b_n = \frac{\Psi_n(mx)\Psi'_n(x) - m\Psi_n(x)\Psi'_n(mx)}{\Psi_n(mx)\xi'_n(x) - m\xi_n(x)\Psi'_n(mx)} \tag{2.2b}$$

Here $\Psi_n$ and $\xi_n$ are Riccati-Bessel functions, $m = n/n_m$ is the contrast parameter, $x = (2\pi R n_m)/\lambda$ is the size parameter and $\lambda$ is the wavelength of the incident field. Once these coefficients are known it is possible to calculate the field everywhere around the sphere. However, it is often convenient to express the overall response in terms of the energy balance between the different mechanisms involved through the scattering and extinction (scattering + absorption) efficiencies:

$$Q_{sca} = \frac{2}{x^2}\sum_{n=1}^{\infty}(2n+1)(|a_n|^2 + |b_n|^2) \tag{2.3a}$$

$$Q_{ext} = \frac{2}{x^2}\sum_{n=1}^{\infty}(2n+1)\,\mathrm{Re}\{a_n + b_n\} \tag{2.3b}$$

Figure 2.3 shows the scattering efficiencies as a function of the sphere dielectric function $\varepsilon$ for a fixed size parameter $x = 0.75$. We can notice enhancement for the electric coefficients in plasmonic materials ($\varepsilon < 0$) while dielectric NPs ($\varepsilon > 0$) show resonances for both electric and magnetic coefficients. These coefficients correspond to surface electric currents ($b_1$, $b_2$, $b_3$) and surface charge distributions ($a_1$, $a_2$, $a_3$) resembling magnetic and electric dipolar, quadrupolar and octupolar configurations [12].

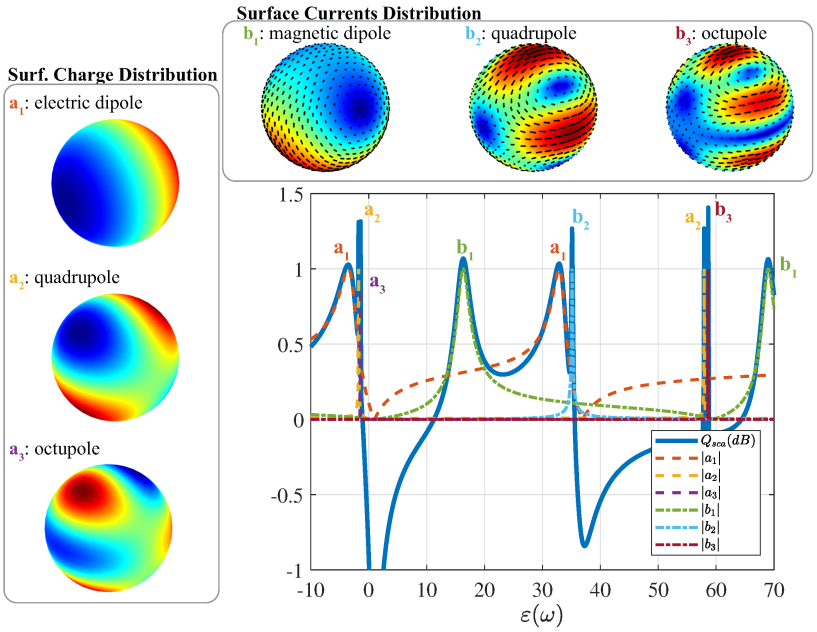


**Figure 2.3:** Scattering efficiencies as a function of $\varepsilon$ for fixed $x = 0.75$, highlighting the contribution of the first three orders of electric and magnetic moments with their corresponding surface charges and currents (taken from [12]).

## Plasmonic nanoparticles

In order to highlight the resonant features of plasmonic NPs, we consider a metallic sphere, sketched in fig. 2.4, characterized by a wavelength-dependent complex valued permittivity $\varepsilon = \varepsilon(\lambda)$, excited by a monochromatic electric field $\mathbf{E}_0$ linearly polarized along the $z$ axis. In the limit of sub-wavelength size of the NP ($R \ll \lambda$), Mie theory can be simplified by applying the Quasi-Static approximation in which we assume that every point of the sphere is excited at the same time so that retardation effects can be neglected. Within this framework, the scattering from the NP can be described through an electrostatic potential $\mathbf{\Phi}$ determined by Laplace equation $\nabla^2\mathbf{\Phi} = 0$. The potential outside the sphere is given by [6]:

$$\Phi_{out} = -E_0 r cos\theta + E_0 \frac{\varepsilon - \varepsilon_m}{\varepsilon + 2\varepsilon_m} \frac{R^3}{r^2} cos\theta \tag{2.4}$$

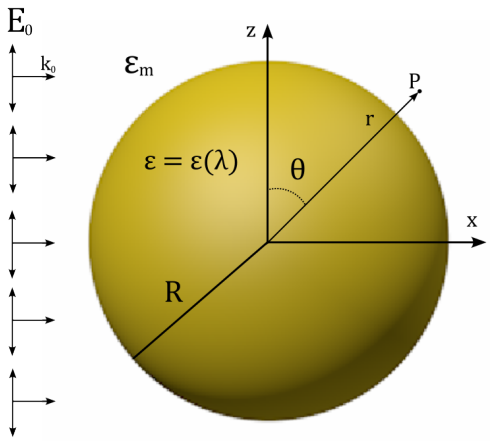


**Figure 2.4:** Metal NP of radius R and permittivity R, embedded in an homogeneous medium with permittivity $\varepsilon_m$ and excited by a linearly polarized monochromatic electric field $E_0$.

where $\theta$ is the polar angle between the position vector $r$ at point $P$ and the $z$ axis. We can notice that $\Phi_{out}$ describes the sum of the potential of the applied field and that of an induced point-like electric dipole $\mathbf{p}$ located in the center of the sphere, expressed as:

$$\mathbf{p} = 4\pi\varepsilon_0\varepsilon_m R^3 \frac{\varepsilon - \varepsilon_m}{\varepsilon + 2\varepsilon_m}\mathbf{E}_0 \tag{2.5}$$

which corresponds to a complex valued polarizability

$$\alpha = 4\pi R^3 \frac{\varepsilon - \varepsilon_m}{\varepsilon + 2\varepsilon_m} \tag{2.6}$$

The polarizability exhibits a resonant enhancement due to the excitation of LSP at the wavelength $\lambda_0$ for which the denominator is minimum. Assuming small $\mathrm{Im}\{\varepsilon\}$, the resonance is achieved when:

$$\mathrm{Re}\{\varepsilon(\lambda_0)\} = -2\varepsilon_m \tag{2.7}$$

known as the *Fröhlich resonance condition*. This behavior is caused by resonant enhancement of the absorption and scattering cross-sections

of the NP which dissipates the LSP energy more efficiently at $\lambda_0$, either by ohmic losses or by emission of radiation due to oscillation of charges [13]. In particular, at resonance, the absorption cross-section radius is much larger than the geometrical one [14].
After excitation, the LSP quickly decays either radiatively by emission of a photon [15] or non radiatively through the generation of high energy electron-hole pairs, known as hot carriers, via Landau damping [16]. The latter mechanism involves the transfer of energy from a plasmon quantum into a single electron-hole pair excitation on a femtosecond timescale and is followed by a series of ultrafast processes [17]. First, in a few hundred femtoseconds, the generated hot carriers redistribute their energy among lower energy electrons via electron-electron scattering. The reduced kinetic energy of these lower-energy electrons results in stronger electron-phonon interactions which gradually bring the electronic distribution to equilibrium within a few picoseconds with consequent increase of the NP temperature. Finally, the equilibration of the lattice, mediated by phonon-phonon interactions over longer timescales ranging from several picoseconds to a few nanoseconds, results in the release of heat into the environment. The ultrafast relaxation processes in plasmonic NPs are inherently linked with variations of their optical properties through nonequilibrium carrier distributions, offering the opportunity to modulate light with unprecedented speeds.

## Mie-resonant nanoparticles

Mie theory shows that Mie-resonant NPs can support different orders of electric and magnetic modes depending on the ratio $\gamma = \lambda/2Rn$. When $\gamma \gg 1$ no resonant modes are excited and the scattering by the particle can be simply described by Rayleigh approximation. The first resonance arises when the particle's diameter is comparable to the wavelength ($\gamma \approx 1$) and corresponds to the excitation of a magnetic dipolar mode. This response results from the strong coupling with cir-

cular displacement currents inside the sphere due to field penetration and retardation effects [18]. Decreasing $\gamma$, at first an electric dipole resonance is formed and then higher order multipoles are excited. The ratio $\gamma$ also shows that in high-index particles different orders of Mie resonances can be excited even for sub-wavelength sizes, a crucial requirement in the realization of metadevices. However, a large value of the refractive index comes at the expense of increased absorption. On this basis, semiconductors represent a versatile choice providing high refractive index at frequencies below the band-gap and relatively low losses [19]. Another important advantage of Mie-resonant NPs is the ability to provide unidirectional scattering. In particular, it was demonstrated that a dielectric sphere with equal electric permittivity and magnetic permeability $\varepsilon = \mu$, referred to as Kerker condition, exhibits zero backscattering [20]. This phenomenon arises from the interference between overlapping electric and magnetic dipole resonances with comparable strength and can be obtained in non-spherical NPs through a proper design of the geometric parameters. Finally, similarly to plasmonic structures, the relaxation of excited carriers in semiconductors is characterized by ultrafast processes which will be explained in detail in chapter 5.

## 2.3 Metasurfaces (MSs)

MSs are two-dimensional optically thin planar arrays of densely packed scatterers having sub-wavelength size and periodicity. These meta-atoms usually consist of highly polarizable resonant NPs made of plasmonic, high permittivity dielectric or semiconductor materials. The presence of inclusions leads to the incident wave being strongly coupled to their near fields resulting in abrupt phase changes that ultimately define the MS scattering properties in the far field. In this way, a suitable choice and arrangement of meta-atoms enables control over

the phase, amplitude and polarization of the reflected and transmitted fields. More interestingly, one can shape light into a desired wavefront by engineering a proper phase gradient along the MS through a spatial variation of the inclusions' geometric parameters such as shape, size and orientation. This is analogous to the operation principle of a phased antenna array where desired field patterns are synthesized by the interference of fields with different phases and amplitudes generated by many closely spaced individual radiative elements [21]. In this sense, the optical response of a MS can be seen as the superposition of spherical wavelets scattered by the meta-atoms that, acting as optical nanoantennas [22], redirect light into anomalous directions. The idea of steering light exploiting customizable phase jumps produced by an array of carefully engineered scatterers was initially proposed by the group of Capasso in a work published in 2011 [23], where they introduced the concept of interface discontinuities which represent one of the first examples of MSs. Considering the system depicted in figure 2.5a, the reflected and transmitted angles are given by the following generalized Snell's laws:

$$n_i \sin(\theta_r) - n_i \sin(\theta_i) = \frac{\lambda_0}{2\pi} \frac{d\phi}{dx} \tag{2.8a}$$

$$n_t \sin(\theta_t) - n_i \sin(\theta_i) = \frac{\lambda_0}{2\pi} \frac{d\phi}{dx} \tag{2.8b}$$

where $\lambda_0$ is the vacuum wavelength and $\phi(x)$ is a continuous space-varying phase term added by the MS on the reflected and refracted waves. These expressions show that by exploiting the additional phase term introduced by the MS one can bend reflected and refracted waves into arbitrary directions. It is also easy to see that the usual Snell laws are retrieved in the case of a constant phase along the surface. A particular case is given by a MS featuring a linear phase gradient. In this case, the MS introduces a constant phase shift bending light without distortion in directions defined by the slope of the phase profile.

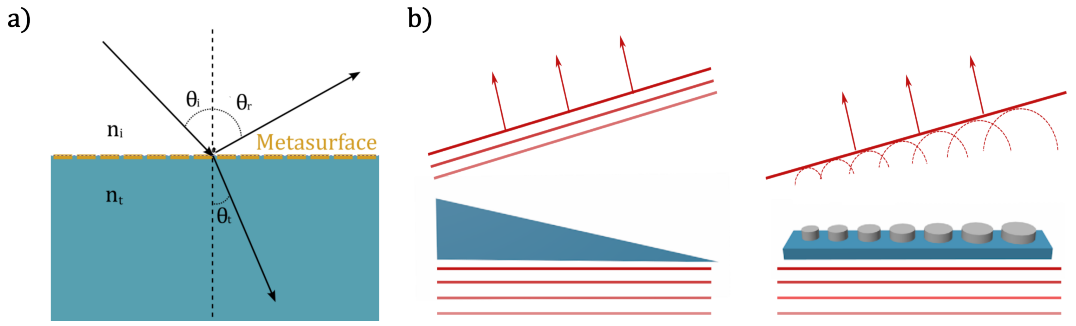


**Figure 2.5:** (a) Anomalous reflection/refraction due to the presence of a MS on the interface between two media. (b) A MS featuring a linear phase gradient transmits light like a refractive prism.

As shown in figure 2.5b, this result is similar to the transmission of a refractive prism. The wavefront of the incident wave will experience at each point along the surface different phase shifts during propagation in the prism due to its variable thickness. By Huygens principle, every point of the surface acts like a secondary source emitting spherical waves. The superposition of all these out-of-phase terms results in a plane wave propagating in the direction where they interfere constructively. The advantage of the MS is that the phase shift is achieved within sub-wavelength scales and the phase profile can be dynamically tuned by an external perturbation that modifies the optical properties of the meta-atoms.
The next sections aim to provide a simple overview of the most relevant aspects of MSs, giving some insight into different characterization methods and classes, followed by a brief discussion on how to achieve dynamic reconfiguration of their static properties and further control over the spectral features of light. Finally, we present some applications focusing on the control of polarization.

## Characterization of metasurfaces

Previously we have seen that bulk MMs can be considered as homogeneous media described by effective parameters obtained by a volumetric average of their microscopic currents. Similarly, a MS can be seen as a 2D homogeneous material characterized by surface-average properties due to its sub-wavelength periodicity and negligible optical thickness. In this picture, a periodic arrangement of meta-atoms is replaced by an equivalent set of electric and magnetic current sheets, characterized by surface current densities, that reflect and transmit light without producing diffracted waves despite the discretized nature of the array. This macroscopic model accurately describes the MS's optical response in the far field even though the fields produced by the two structures are very different near the surface [24]. The optical properties of the MS can be then retrieved by applying models that relate the surface currents to the incident and scattered fields through a set of properly defined boundary conditions resulting in reflection and transmission coefficients expressed as functions of some effective parameters [25]. A conventional approach consists in modeling the surface averaged currents as induced electric and magnetic dipole moments in the meta-atoms and relating them to the incident fields via effective polarizability tensors. In this case, the MS can be seen as an equivalent array of dipolar sources that radiates plane waves in the surrounding space. The advantage of this model is that the polarizabilities can be easily related to the geometry of the meta-atom. In this way, it provides a link between the single unit cell response and the net scattering behavior of the whole structure, thus representing a powerful tool in the design of MSs with desired properties. Alternatively, the MS can be characterized by modeling the discontinuities along the surface using impedance and admittance as effective parameters or by relating the induced surface currents to the tangential electric and magnetic field through susceptibilities. The macroscopic nature

of these quantities allows a more intuitive interpretation of the MS behavior but does not provide insight into which geometry is needed to achieve a certain response.

## Classification of metasurfaces

There is not a unique way to classify MSs. For example, we can distinguish different classes depending on the frequency operation regime (microwave and optical), the ability to tune their static response (passive and active), the spatial features of the array (homogeneous and inhomogeneous), or the spatial localization/delocalization of their resonance (local and nonlocal). Another possible classification is based on the response of the meta-atoms upon normally incident plane-wave illumination which is particularly useful since it provides insight into the drawbacks inherent to using certain materials and geometries [26]. Inclusions featuring a purely electric dipole response, typically observed in plasmonic materials, present several limitations. If the response is isotropic the maximum phase achievable is $\pi$ while $2\pi$ shifts are needed to have complete control on the scattered wavefront. The full $2\pi$ space can be covered by employing orthogonally oriented anisotropic meta-atoms (fig. 2.6a) that introduce an additional $\pi$ shift in the cross-polarized component of the scattered field. However, conversion efficiencies are typically very low and most of the light is radiated in ordinary directions. Alternatively, $2\pi$ modulations can be obtained in MSs that implement Metal-Insulator-Metal (MIM) inclusions consisting of closely spaced plasmonic nanoantennas with a dielectric in between that acts as a resonator. The strong coupling between the two metallic layers leads to the generation of high and low energy modes characterized by in-phase and out-of-phase polarization currents resulting in electric and magnetic dipole moments, respectively [26] (fig. 2.6b). Better control can be achieved with dielectric meta-atoms exhibiting Mie resonances. Contrary to plasmonic materials where the

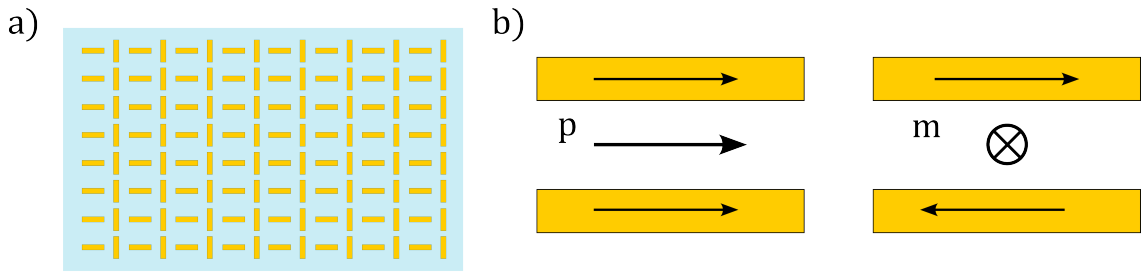


**Figure 2.6:** (a) Example of plasmonic MS for full $2\pi$ phase coverage. (b) Resonant modes in MIM NP: in-phase and out-of-phase surface currents generate electric and magnetic dipole moment response respectively.

excited modes are confined on the surface, in dielectrics the field penetrates deeply so that the NP forms a resonator by itself enabling the generation of both electric and magnetic moments within a single layer. An important case is given by structures featuring inclusions with overlapping electric and magnetic resonances, known as Huygens MSs, that result in forward dominant scattering leading to full transmission and $2\pi$ phase shifts. The improvement obtained in this case can be directly linked to Huygens principle [27] which states that the field distribution around a confined surface is totally determined by the electric and magnetic components tangential to the surface, meaning that both electric and magnetic responses of comparable strengths are needed to arbitrarily shape a wavefront.

## Active metasurfaces

We have seen that a proper arrangement of meta-atoms provides control over the phase, amplitude and polarization of the scattered fields, enabling the structuring of light in a predefined manner. However, the optical response is inherently linked to fixed properties of the array, limiting the possibility to achieve functionalities that require devices capable of varying their features dynamically during operation. For

example, scanning devices require the ability to implement a phase gradient that can be dynamically reconfigured at will by some external control [28]. In this context, active MSs open up new opportunities as tunable devices for a wide variety of applications, setting also new challenges in the development of efficient reconfiguration mechanisms. In general, MSs can be tuned by properly changing the properties of the lattice, the substrate or the individual meta-atoms [29]. These changes are obtained through the application of an external perturbation that modifies either the structural features of the system by mechanical means, or the optical properties of the materials composing the MS. The latter can be achieved by acting directly on the meta-atoms or by implementing reconfigurable materials that interact with them.
A particularly important approach in the reconfiguration of MSs consists in tuning their optical properties by exploiting an external optical stimulus [30]. Usually, a strong ultrashort pump pulse is used to produce a nonequilibrium carrier distribution in the meta-atoms resulting in photo-induced transient modulation of the refractive index. This, combined with the ultrafast relaxation processes typical of NPs, offers the possibility to realize devices in which the optical response can be transiently modified by all-optical means on ultrashort timescales with very high efficiency.

## Nonlocal metasurfaces

The above mentioned classes of MS can be labeled as local in the sense that they feature inclusions that exhibit strong confinement of the excited modes, resulting in individual optical responses mainly localized in the single unit cell with no interaction between the near fields of adjacent meta-atoms. The engineering of a local response has been for many years the conventional approach in the realization of MSs since it allows straightforward designs of arrays in which each scatterer is independently tailored to apply a specific transformation without af-

fecting the behavior of the others. However, having a strongly localized response in the real space leads to a broadband response in the reciprocal space limiting the possibility to achieve frequency and angle selectivity which are desirable in many applications. On the other hand, spectral control can be achieved in structures having extended or propagating modes supported by sub-wavelength period gratings that act as leaky waveguides. In these nonlocal devices, the interaction between meta-atoms leads to the near fields being coupled to the external waves only for those frequencies that match the dispersion relation of these modes, resulting in a delocalized response characterized by sharp resonances. In this case, the narrowband response in the momentum space precludes the ability to tailor a desired wavefront on the scattered light. Simultaneous control over spectral and spatial features of the scattered light can be obtained in structures exploiting larger periodicities to redirect resonantly excited modes into different diffraction orders. These diffractive nonlocal devices combine both the wave-shaping functionalities of local MSs and the frequency selectivity of nonlocal devices, thus representing the most general class of MSs.

## Applications of metasurfaces

MSs are now used in a wide variety of applications either as flat compact alternatives to bulk optical elements, such as lenses [31] and polarization optics [32], or to achieve completely new functionalities like cloaking [33]. Given the scope of this work, in this section we focus on the ability to control the polarization state of light by exploiting homogeneous arrays of resonant scatterers.

Control of polarization is typically achieved with devices such as polarizers, used to selectively transmit one state of polarization while rejecting others, and waveplates, enabling conversion between different polarization states. Conventional waveplates are based on the relative phase shift between orthogonally polarized electric fields accumu-

lated through propagation in birefringent media. However, due to the low birefringence of natural materials, polarization conversion requires propagation over distances much longer than the wavelength, precluding the development of miniaturized devices suitable for nanophotonic applications. Moreover, active reconfiguration of conventional polarization optics relies on electric actuators, limiting the performances of polarization-switching devices to gigahertz modulation speeds. In this context, MSs have been proposed as efficient ultrafast polarization selective components in which giant birefringent and dichroic features can be synthesized and modulated on a picosecond timescale by all-optical means [34]. Artificial birefringence and dichroism can be engineered by exploiting homogeneous arrays of anisotropic inclusions characterized by a large aspect ratio, such as nanorods or nanowires, where the main interaction with external fields occurs for polarization states parallel to the long axis of the meta-atoms, which directly translates into a dichroic response. Indeed, as previously discussed, the resonant modes in NPs are highly dependent on their geometric parameters. Therefore, by carefully adjusting the length and width of the meta-atom, one can independently control the phase shift impressed on two orthogonally polarized electric fields achieving the waveplate functionality over sub-micrometer distances. Additionally, the anisotropic features of these devices might be tuned by an external optical stimulus enabling terahertz polarization-switching speeds.

# Chapter 3

# Introduction to ultrafast spectroscopy

Ultrafast spectroscopy refers to a set of experimental techniques that employ ultrashort laser pulses to study the relaxation dynamics of photoinduced processes with a temporal resolution only limited by the pulse duration [35]. In recent years, incredible advances in the generation of ultrashort pulses have pushed the sensitivity of these techniques to lower and lower limits. The simplest technique in this field of research is called pump-probe and consists in the use of a resonant strong pulse (pump) to induce population changes in a sample, which are then monitored by a weaker pulse (probe) at variable time delays with respect to the excitation. This chapter aims to provide the theoretical background necessary to understand the results of a pump-probe measurement and the different nonlinear processes involved in the generation of the ultrashort pulses required for this technique. A short introduction to pulse propagation in nonlinear media is followed by a discussion of second and third order nonlinear effects, in particular Second Harmonic Generation (SHG), broadband pulse amplification by means of Optical Parametric Amplification (OPA) and generation of ultrabroadband pulses achieved through White Light Generation

(WLG). Finally the different signals arising in a pump-probe experiment are explained together with their physical interpretation.

## 3.1 Pulse propagation in nonlinear media

In order to describe pulse propagation in optical media we start from Maxwell's equations:

$$\nabla \cdot \mathbf{D} = \rho \tag{3.1a}$$

$$\nabla \cdot \mathbf{B} = 0 \tag{3.1b}$$

$$\nabla \times \mathbf{E} = -\frac{\partial \mathbf{B}}{\partial t} \tag{3.1c}$$

$$\nabla \times \mathbf{H} = \mathbf{J} + \frac{\partial \mathbf{D}}{\partial t} \tag{3.1d}$$

where $\mathbf{E}$ is the electric field, $\mathbf{D}$ is the electric displacement field, $\mathbf{B}$ is the magnetic flux density, $\mathbf{H}$ is the magnetic field, $\mathbf{J}$ is the total electric current density, $\rho$ is the total electric charge density and $\mu_0$ is the vacuum permeability.
In addition we have the constitutive laws linking magnetic and electric fields:

$$\mathbf{D} = \varepsilon_0 \mathbf{E} + \mathbf{P} \tag{3.2a}$$

$$\mathbf{B} = \mu_0(\mathbf{H} + \mathbf{M}) \tag{3.2b}$$

$$\mathbf{P} = \varepsilon_0 \chi \mathbf{E} \tag{3.2c}$$

$$\mathbf{H} = \chi_m \mathbf{M} \tag{3.2d}$$

where $\mathbf{P}$ is the polarization field, $\mathbf{M}$ is the magnetization field, $\varepsilon_0$ is the vacuum permittivity, while $\chi$ and $\chi_m$ are respectively the electric and magnetic susceptibilities of the medium. By applying the rotor operator to both sides of (3.1c) one can retrieve the exact propagation

equation:

$$\nabla \times (\nabla \times \mathbf{E}) + \frac{1}{c^2}\frac{\partial^2 \mathbf{E}}{\partial t^2} = -\mu_0 \frac{\partial}{\partial t}(\nabla \times \mathbf{M}) - \mu_0 \frac{\partial \mathbf{J}}{\partial t} - \mu_0 \frac{\partial^2 \mathbf{P}}{\partial t^2} \quad (3.3)$$

This equation can be simplified by considering non magnetic ($\chi_m = 0$), source-free ($\rho = 0,\ \mathbf{J} = 0$) and homogeneous ($\nabla \cdot \mathbf{E} = 0$) media. Furthermore, we consider the pulse to be linearly polarized and propagating along the z direction (scalar approximation), with no variation along the x-y plane (plane wave approximation). Under these assumptions, the propagation equation becomes:

$$\frac{\partial^2 E(z,t)}{\partial z^2} - \frac{1}{c^2}\frac{\partial^2 E(z,t)}{\partial t^2} = \mu_0 \frac{\partial^2 P(z,t)}{\partial t^2} \quad (3.4)$$

The result is a wave equation having the polarization acting as a source: the electric dipoles in the medium will respond to the incoming field oscillating and thus emitting electromagnetic waves. In the most general case the polarization can be split up into the sum of linear and nonlinear contributions $P(z,t) = P^{(l)}(z,t) + P^{(nl)}(z,t)$ where the linear part is proportional to the electric field and can be expressed as:

$$P^{(l)}(z,t) = \varepsilon_0 \chi(\omega) E(z,t) = \varepsilon_0 [\varepsilon_r(\omega) - 1] E(z,t) \quad (3.5)$$

where $\varepsilon_r(\omega)$ is the relative permittivity of the medium, which in general is a function of frequency. It is now useful to rewrite equation (3.4) in the frequency domain. By applying the Fourier transform to both sides and inserting the expression for the linear component of the polarization we obtain:

$$\frac{\partial^2 \tilde{E}(z,\omega)}{\partial z^2} + \frac{\omega^2}{c^2}\varepsilon_r(\omega)\tilde{E}(z,\omega) = -\mu_0 \omega^2 \tilde{P}^{(nl)}(z,\omega) \quad (3.6)$$

It is possible to express the electric field and the nonlinear polarization in terms of slowly varying amplitude functions multiplied by a carrier

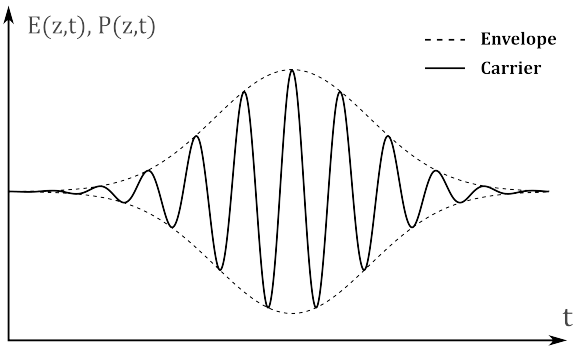


**Figure 3.1:** Envelope representation of a pulse

(see figure 3.1):

$$E(z,t) = \mathrm{Re}\left\{A(z,t)e^{i(\omega_0 t - k_0 z)}\right\} \tag{3.7a}$$

$$P(z,t) = \mathrm{Re}\left\{B(z,t)e^{i(\omega_0 t - k_p z)}\right\} \tag{3.7b}$$

Having defined the fields this way, their Fourier transforms are simply given by the spectrum of the envelope centered on the carrier frequency and multiplied by a spatial phase factor:

$$\tilde{E}(z,\omega) = e^{-ik_0 z}\tilde{A}(z,\omega-\omega_0) \tag{3.8a}$$

$$\tilde{P}^{(nl)}(z,\omega) = e^{-ik_p z}\tilde{B}(z,\omega-\omega_0) \tag{3.8b}$$

Inserting these expressions into the wave equation we get:

$$\left(\frac{\partial^2\tilde{A}}{\partial z^2} - 2ik_0\frac{\partial\tilde{A}}{\partial z} - k_0^2\tilde{A} + \frac{\omega^2}{c^2}\varepsilon_r(\omega)\tilde{A}\right)e^{ik_0 z} = -\mu_0\omega^2\tilde{B}e^{-ik_p z} \tag{3.9}$$

This expression can be simplified by assuming that the envelope does not vary significantly during propagation over distances of the order of the wavelength. This is called Slowly Varying Envelope Approximation (SVEA) and allows us to neglect the second derivative of the envelope. We introduce the dispersion relation $k(\omega)$, defined as $k^2(\omega) = \frac{\omega^2}{c^2}\varepsilon_r(\omega)$,

which expresses how much phase shift each frequency component of the spectrum experiences during propagation. The equation becomes:

$$\frac{\partial \tilde{A}}{\partial z} + \frac{i}{2k_0}\Big[k^2(\omega) - k_0^2\Big]\tilde{A} = -\frac{i\mu_0\omega_0^2}{2k_0}Be^{-i\Delta kz} \tag{3.10}$$

where we have introduced the quantity $\Delta k = k_p - k_0$, called wave-vector mismatch. As we will see, this quantity plays a key role in the efficiency of nonlinear processes since having input field and nonlinear polarization phase-matched ($\Delta k = 0$) will result in constructive interference between the two. In the framework of the SVEA it is possible also to assume $k + k_0 \approx 2k_0$, which is equivalent to neglecting any back-propagating wave. As a consequence, we get that $k^2(\omega) - k_0^2 = (k(\omega) - k_0)(k(\omega) + k_0) \approx 2k_0(k(\omega) - k_0)$ and the equation becomes:

$$\frac{\partial \tilde{A}}{\partial z} + i\Big[k(\omega) - k_0\Big]\tilde{A} = -\frac{i\mu_0\omega_0^2}{2k_0}\tilde{B}e^{-i\Delta kz} \tag{3.11}$$

where we have also assumed that the nonlinear polarization varies slowly over the timescale of an optical cycle ($\omega^2\tilde{B} \approx \omega_0^2\tilde{B}$). If the dispersion relation is slowly varying over the pulse spectrum it can be approximated by its Taylor series expansion around $\omega_0$. Stopping at the second order we get:

$$\begin{aligned} k(\omega) &\approx k_0 + \frac{\partial k}{\partial \omega}\bigg|_{\omega=\omega_0}(\omega - \omega_0) + \frac{1}{2}\frac{\partial^2 k}{\partial \omega^2}\bigg|_{\omega=\omega_0}(\omega - \omega_0)^2 = \\ &= k_0 + \frac{(\omega - \omega_0)}{v_g} + \frac{GVD}{2}(\omega - \omega_0)^2 \end{aligned} \tag{3.12}$$

where $v_g$ is the group velocity, describing the speed at which the peak of the pulse travels, and $GVD$ is the group velocity dispersion, which takes into account the effect of dispersion during propagation, together with higher order terms. This approximation allows to easily compute

the inverse Fourier transform, leaving us with:

$$\frac{\partial A}{\partial z} + \frac{1}{v_g}\frac{\partial A}{\partial t} - i\frac{GVD}{2}\frac{\partial^2 A}{\partial t^2} = -\frac{i\mu_0\omega_0^2}{2k_0}\tilde{B}e^{-i\Delta kz} \tag{3.13}$$

Again we find a forced wave equation where the nonlinear polarization acts as a source, generating waves with the same frequency and phase as the electric field propagating inside of the medium.
For the moment we will shortly focus on linear propagation by neglecting the nonlinear polarization in order to explain the effect of dispersion. By considering a reference frame moving with the pulse we can rewrite equation (3.13) as follows:

$$\frac{\partial A}{\partial z} - i\frac{GVD}{2}\frac{\partial^2 A}{\partial t^2} = 0 \tag{3.14}$$

from which is clear that in non-dispersive materials ($GVD = 0$) the pulse remains unchanged during propagation. By means of the superposition principle, the envelope can be seen as the sum of many wave packets centered on different frequencies. Since in general the refractive index of a medium is a function of frequency, each wave packet will travel at a different speed, with the faster moving towards the front of the pulse and the slower towards the back, accumulating a reciprocal delay and eventually leading to a broadening of the pulse. The relative displacement of the different frequency components inside of the pulse will also cause a time dependence of its instantaneous frequency known as chirp. We can then understand the first order approximation as the situation in which either the pulse spectrum is narrow enough or the propagation distances short enough that the delay accumulated, therefore the broadening, is negligible. When this is not the case, higher order terms must be considered. As an example we can consider a Gaussian pulse, having its envelope defined as:

$$A(0,t) = A_0 e^{-\frac{t^2}{2\tau_p^2}} \tag{3.15}$$

The pulse duration can be estimated by its FWHM given by $\Delta t = \tau_p\sqrt{2ln2}$. Solving equation (3.14) for the envelope we can determine its evolution during propagation, finding that after a propagation distance L the FWHM changes to:

$$\Delta t' = \Delta t\sqrt{1+\left(\frac{GVD\cdot L}{\tau_p^2}\right)^2} = \Delta t\sqrt{1+\left(\frac{L}{L_D}\right)^2} \tag{3.16}$$

where we have introduced the quantity $L_D = \tau_p^2/GVD$ called dispersion length. If $L << L_D$ the effect of broadening is negligible and $\Delta t' \approx \Delta t$, while if $L >> L_D$ then $\Delta t' \approx \Delta t(L/L_D)$ and the pulse duration scales linearly with the propagation distance L. This also shows that the larger the initial duration of the pulse the more dispersion it experiences during propagation.
In the following sections, we will make use (3.13) to describe the effects arising from the propagation of light in nonlinear media. In doing so, we will only consider the perturbative regime in which the departures from linearity are small so that the polarization can be expressed as a power series of the electric field:

$$P = \varepsilon_0\left(\chi^{(1)}E + \chi^{(2)}E^2 + \chi^{(3)}E^3 + \cdots\right) \tag{3.17}$$

where $\chi^{(n)}$ are the $n^{th}$ order susceptibilities of the medium. As the intensity of the field increases, the nonlinear terms start becoming increasingly important and the polarization drifts from its linear behavior. For our purposes, we will restrict this discussion to second and third order nonlinear effects. It is important to note that while any media without particular symmetry restrictions shows third order nonlinearities for sufficiently high intensities, the $\chi^{(2)}$ term is non-zero only in non-centrosymmetric materials.

## 3.2 Second order nonlinear effects

We want now to discuss the nonlinear interaction among waves propagating inside of a non-centrosymmetric medium, in which the nonlinear polarization is proportional to the square of the electric field:

$$P^{(2)} = \varepsilon_0 \chi^{(2)} E^2 \tag{3.18}$$

Expressing the electric field as the superposition of two propagating pulses with amplitudes $A_1(z,t)$ and $A_2(z,t)$, having carrier frequencies $\omega_1$ and $\omega_2$ respectively, we find that the nonlinear polarization will mix the waves producing fields at frequencies $2\omega_1, 2\omega_2, \omega_1+\omega_2, \omega_2-\omega_1$ plus a DC component, as shown in figure 3.2. These processes are called:

- **Second Harmonic generation (SHG):** each wave interacts with itself generating a new component with twice the frequency of the initial one.
- **Sum Frequency Generation (SFG):** the interaction between waves at frequencies $\omega_1$ and $\omega_2$ results into a new component oscillating at $\omega_3 = \omega_1 + \omega_2$.
- **Difference Frequency Generation (DFG):** waves at frequencies $\omega_3$ and $\omega_1$ interact to produce a new wave at frequency $\omega_2 = \omega_3 - \omega_1$.
- **Optical Rectification (OR):** each wave interacts with itself to produce a constant signal.

In general, this situation can be described by a system of three interacting waves at frequency $\omega_1, \omega_2, \omega_3 = \omega_1 + \omega_2$. This treatment is usually called three-wave mixing. The electric field can be then expressed as:

$$\begin{aligned} E(z,t) = \mathrm{Re}\Big\{ (A_1(z,t)e^{i(\omega_1 t - k_1 z)} + A_2(z,t)e^{i(\omega_2 t - k_2 z)} + \\ + A_3(z,t)e^{i(\omega_3 t - k_3 z)} \Big\} \end{aligned} \tag{3.19}$$

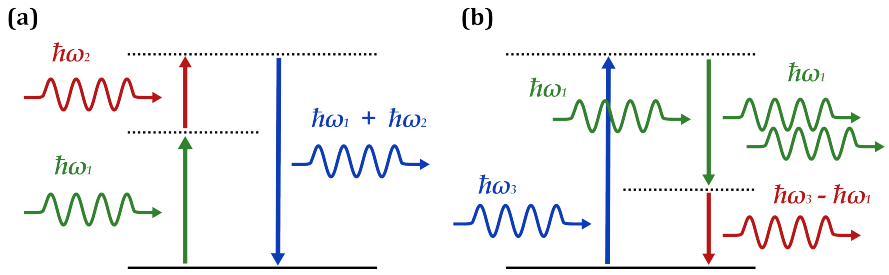


**Figure 3.2:** Energy level scheme of second order nonlinear interactions: (a) Sum Frequency Generation (SFG), (b) Difference Frequency Generation (DFG). SHG and OR can be seen in the picture as particular cases of SFG and DFG, respectively, in which the input waves have the same frequency.

The resulting nonlinear polarization at frequencies $\omega_1, \omega_2, \omega_3$ is given by:

$$P^{(2)}_{\omega_1}(z,t) = \varepsilon_0 \chi^{(2)} \,\mathrm{Re}\left\{A_3 A_2^* e^{i[\omega_1 t - (k_3 - k_2)z]}\right\} \tag{3.20a}$$

$$P^{(2)}_{\omega_2}(z,t) = \varepsilon_0 \chi^{(2)} \,\mathrm{Re}\left\{A_3 A_1^* e^{i[\omega_2 t - (k_3 - k_1)z]}\right\} \tag{3.20b}$$

$$P^{(2)}_{\omega_3}(z,t) = \varepsilon_0 \chi^{(2)} \,\mathrm{Re}\left\{A_1 A_2 e^{i[\omega_3 t - (k_1 + k_2)z]}\right\} \tag{3.20c}$$

We can notice that each frequency component of the polarization is proportional to the amplitudes of waves oscillating at different frequencies, showing how the nonlinearity mediates the transfer of energy between them. The nonlinear polarization will also contain terms oscillating at other frequencies. However, we assume that only the interaction at $\omega_1$, $\omega_2$ and $\omega_3$ is efficient due to phase-matching conditions. Inserting these results into the nonlinear propagation equation, neglecting dispersion effects and assuming monochromatic waves, we

obtain a system of coupled equations for the three envelopes:

$$\frac{\partial A_1}{\partial z} = -id_1 A_3 A_2^* e^{-i\Delta kz} \tag{3.21a}$$

$$\frac{\partial A_2}{\partial z} = -id_2 A_3 A_1^* e^{-i\Delta kz} \tag{3.21b}$$

$$\frac{\partial A_3}{\partial z} = -id_3 A_1 A_2 e^{i\Delta kz} \tag{3.21c}$$

where we have defined the nonlinear coupling coefficients $d_i = \frac{\omega_i \chi^{(2)}}{4cn_i}$ and the wave-vector mismatch $\Delta k = k_3 - k_1 - k_2$. These equations allow to describe many second order nonlinear processes.

## 3.3 Second Harmonic Generation (SHG)

Second Harmonic Generation (SHG) is a process in which a field oscillating at frequency $\omega$, called fundamental frequency, interacts with a non-centrosymmetric material to produce a new wave oscillating at $2\omega$, called second harmonic. We can treat this particular case starting from the coupled equations and taking as input intensities $I_1 = I_2 = I_\omega/2$, resulting in $A_1 = A_2 = A_\omega/\sqrt{2}$. Since the first two equations become redundant, the system simplifies to:

$$\frac{\partial A_\omega}{\partial z} = -id_\omega A_\omega^* A_{2\omega} e^{-i\Delta kz} \tag{3.22a}$$

$$\frac{\partial A_{2\omega}}{\partial z} = -i\frac{d_{2\omega}}{2} A_\omega^2 e^{i\Delta kz} \tag{3.22b}$$

We proceed by making the non-depletion approximation, where we assume that the fundamental remains constant during propagation and doesn't deplete while generating the second harmonic. Of course this approximation violates energy conservation but can still be valid when the conversion efficiency is low. Solving (3.22b) we get:

$$I_{2\omega}(z) = |A_{2\omega}(z)|^2 = \frac{d_{2\omega}^2}{4} I_\omega(0)^2 z^2 sinc^2\Big(\frac{\Delta kz}{2}\Big) \tag{3.23}$$

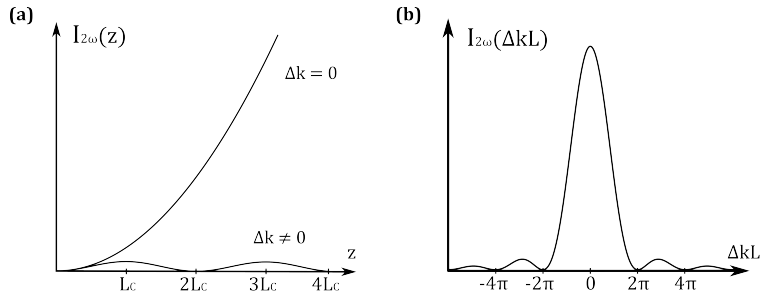


**Figure 3.3:** (a) Second harmonic intensity as a function of propagation distance inside the crystal. (b) Second harmonic intensity as a function of the phase mismatch.

As shown in figure 1.3a, we find that the second harmonic intensity increases quadratically throughout propagation when $\Delta k = 0$, the so called phase-matching condition, while for $\Delta k \neq 0$ it shows an oscillatory trend of period $2L_C = 2\pi/\Delta k$, where $L_C$ is the minimum distance for which the intensity of the second harmonic is maximum and is called coherence length. In this case, the maximum intensity achievable depends on the value of the phase mismatch, as can be seen in figure 3.3b: the bigger $\Delta k$, the lower the conversion efficiency. We can understand this situation by considering the nonlinear polarization described by the system (3.20): we notice that the component oscillating at $\omega$ is driven by the amplitude of the second harmonic, therefore in general during propagation we expect the nonlinear polarization to mediate the exchange of energy in both directions. This is due to the fact that the phase mismatch between second harmonic and nonlinear polarization is not constant along the length of the crystal so that also the way they interfere with each other changes as they propagate, resulting in a periodic reversal of the energy transfer direction. However, when phase matching conditions are satisfied, the fields are always in phase so that the process will only result in constructive interference between partial second harmonic generated inside the medium, making this conversion the only efficient one. The phase matching condition

is achieved when $\Delta k = k_{2\omega} - 2k_{\omega} = 0$, which translates into:

$$n(2\omega) = n(\omega) \tag{3.24}$$

This is not possible in isotropic materials since their refractive index increases monotonically with frequency. Instead, the phase matching condition is usually satisfied with birefringent materials in which the refractive index experienced by the waves depends both on their polarization state and propagating direction. A typical crystal used for SHG is beta-barium borate (BBO). When phase matching can't be achieved, we can still maximize the efficiency by keeping $\Delta k$ as small as possible and choosing the crystal length equal to $L_C$.

## 3.4 Optical Parametric Amplification (OPA)

Optical Parametric Amplification (OPA) is a DFG process in which the field oscillating at frequency $\omega_1$ is much weaker than the one at frequency $\omega_3$. In this process an intense beam at $\omega_3$ (pump) transfers energy to the beam at $\omega_1$ (signal) amplifying it, and generates light at $\omega_2$ (idler) as a consequence of energy conservation. This method therefore offers the ability of tuning a fixed frequency laser system over a broad range of wavelengths. In order to understand the operation principle of an OPA, we will start considering parametric amplification for monochromatic waves and then extend the results to the case of broadband pulses. Starting from the coupled equations and assuming no pump depletion ($A_3 \approx constant$) and no idler beam at the beginning ($A_2(0) = 0$), it is possible to derive the following differential equation:

$$\frac{\partial^2 A_1}{\partial z^2} = -i\Delta k \frac{\partial A_1}{\partial z} + \Gamma^2 A_1 \tag{3.25}$$

where $\Gamma^2 = d_1 d_2 |A_3|^2$. After the interaction distance L, the signal intensity is:

$$I_1(L) = I_1(0)\left[1 + \left(\frac{\Gamma}{g} sinh(gL)\right)^2\right] \tag{3.26}$$

where: $g = \sqrt{\Gamma^2 - \frac{\Delta k^2}{4}}$ is the small signal gain. We can define the parametric gain of the process G(L) as:

$$G(L) = \frac{I_1(L)}{I_1(0)} = \left[1 + \left(\frac{\Gamma^2}{g^2} sinh(gl)\right)^2\right] \tag{3.27}$$

from which is evident that the gain is maximum when $\Delta k = 0$, making it clear that the phase-matching condition is essential to have efficient amplification. In the large gain limit ($gL >> 1$) we have:

$$I_1(L) \approx I_1(0)\left(\frac{\Gamma}{g}\right)^2 \frac{e^{2gL}}{4} \tag{3.28a}$$

$$G(L) \approx \left(\frac{\Gamma}{g}\right)^2 \frac{e^{2gL}}{4} \tag{3.28b}$$

We see that in the large gain limit and within the non depletion approximation the signal grows exponentially with the interaction length L, showing that the OPA behaves like a real amplifier. However, this mechanism is fundamentally different from classical optical amplifiers based on population inversion: it does not have storage capacity, the gain center frequency is not fixed but depends on the phase-matching condition and the gain bandwidth is not limited by the transition linewidth but only by the range of frequencies over which phase-matching can be achieved. This exponential gain is also very different from the quadratic increase we encountered in SHG. Thanks to the symmetry in the coupled equations for signal and idler, also the idler can be amplified by the pump, generating signal photons and thus resulting in a positive feedback mechanism which gives rise to the exponential gain.

Until now we have limited our discussion to the case of monochromatic waves and we have seen that the main limitations in performances arise from the phase mismatch $\Delta k$. In the case of broadband pulse amplification, two additional constraints must be considered. The first one is given by the bandwidth over which this amplification process is actually effective, called phase-matching bandwidth, which can be calculated as follows. We define the maximum tolerable phase mismatch $\Delta k_m$ as the one for which $G(\Delta k_m) = \frac{1}{2}G(\Delta k = 0)$. This leads to:

$$\Delta k = 2\sqrt{ln(2)\frac{\Gamma}{L}} \tag{3.29}$$

If we now consider a system of three phase-matched frequencies $\bar{\omega}_1, \bar{\omega}_2, \bar{\omega}_3$ we can calculate the phase mismatch $\Delta k$ relative to a detuning $\Delta\omega$ such that $\bar{\omega}_3 = \omega_3$, $\bar{\omega}_2 = \omega_2 + \Delta\omega$, $\bar{\omega}_1 = \omega_1 - \Delta\omega$ by simply expanding $\Delta k$ in Taylor series up to the first order, obtaining $\Delta k = \delta_{12}\Delta\omega$, where $\delta_{12} = v_{g1}^{-1} - v_{g2}^{-1}$ is the group velocity mismatch between idler and signal. We are left with the following expression for the gain bandwidth:

$$\Delta\omega_{FWHM} = \frac{4}{\delta_{12}}\sqrt{ln(2)\frac{\Gamma}{L}} \tag{3.30}$$

from which is clear that the smaller $\delta_{12}$ the greater the bandwidth over which we have good amplification. In the case of degenerate OPA ($\delta_{12} = 0$), the expression diverges, suggesting that a first order approximation is no longer valid. Expanding $\Delta k$ up to the second order we get:

$$\Delta k = \delta_{12}\Delta\omega - \frac{1}{2}\Big[GVD_1 + GVD_2\Big]\Delta\omega^2 \tag{3.31}$$

and the corresponding bandwidth is:

$$\Delta\omega = \frac{2}{\sqrt{|GVD_1 + GVD_2|}}\sqrt[4]{ln(2)\frac{\Gamma}{L}} \tag{3.32}$$

The bandwidth achieved under these conditions is usually very large but the requirement of having idler and signal frequencies equal makes this configuration not suitable for many applications. Luckily it is possible to achieve broadband amplification even outside of degeneracy by introducing a new degree of freedom represented by the direction of propagation of the three interacting waves. This process is called Non-collinear Optical Parametric Amplification (NOPA) and the broadband is achieved when:

$$v_{g2} = v_{g1} cos(\Omega) \tag{3.33}$$

where $\Omega$ is the angle between signal and idler propagation directions. This allows to simultaneously fulfill the phase-matching conditions for a very wide range of signal frequencies resulting in a broadband amplification.
The second limitation arises from the temporal walk-off between pulses due to the relative group delay that they accumulate during propagation. Given a pump pulse with FWHM $\tau$, we call pulse-splitting length the distance after which the signal is no longer temporally overlapped to the pump, defined as:

$$l_{j3} = \left| \frac{\tau}{\delta_{j3}} \right| = \left| \frac{\tau}{v_{gj} - v_{g3}} \right| \qquad j = 1, 2 \tag{3.34}$$

In order to understand which condition will give us the best temporal overlap between pulses we can consider two situations:

- $\boldsymbol{\delta_{13}\delta_{23} > 0}$: in this case, both the signal and idler are either faster or slower than the pump. Therefore they walk away from the pump in the same direction and the maximum length over which the parametric amplification takes place is the pulse splitting-length.

- $\boldsymbol{\delta_{13}\delta_{23} < 0}$: this case describes the situation in which either the signal or idler is faster than the pump while the other is slower,

thus they walk away in different directions. The signal interacting with the pump will generate idler photons which, traveling in the opposite direction, will stimulate the emission of signal photons, resulting in a feedback mechanism that will last over distances longer than the pulse-splitting length.

## 3.5 Third order nonlinear effects

As we have seen, centrosymmetric materials respond with a linear polarization for moderate intensity input fields. For higher powers the third order nonlinear term starts to become non negligible, introducing a time dependent nonlinear modulation of the refractive index. This is known as Kerr effect and can be derived by considering a nonlinear polarization in the form:

$$P(z,t) = P^{(1)}(z,t) + P^{(3)}(z,t) = \varepsilon_0\Big(\chi^{(1)}E(z,t) + \chi^{(3)}E^3(z,t)\Big) \quad (3.35)$$

By inserting the electric field we obtain:

$$P(z,t) = \varepsilon_0\left[\chi^{(1)} + \frac{3\chi^{(3)}}{4}|A|^2\right]\mathrm{Re}\left\{A(z,t)e^{i(\omega_0 t - k_0 z)}\right\} \quad (3.36)$$

The quantity in square brackets can be seen now as the effective susceptibility of the medium, considering also nonlinear terms. Reminding that the electric susceptibility and the refractive index of the material are linked by $n^2 = 1 + \chi$, we can write:

$$n^2 = 1 + \chi^{(1)} + \frac{3\chi^{(3)}}{4}|A|^2 = n_0^2 + \frac{3\chi^{(3)}}{4}|A|^2 \quad (3.37)$$

where $n_0$ is the linear refractive index of the medium. By taking the square root and assuming the nonlinear term to be much smaller than $n_0^2$ we arrive at:

$$n = n_0\sqrt{1 + \frac{3\chi^{(3)}}{4n_0^2}|A|^2} \approx n_0\left(1 + \frac{3\chi^{(3)}}{8n_0^2}|A|^2\right) = n_0 + \frac{3\chi^{(3)}}{8n_0}|A|^2 \quad (3.38)$$

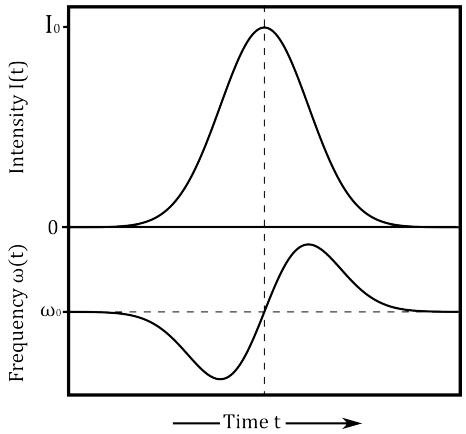


**Figure 3.4:** Intensity dependent spectral broadening of the pulse caused by SPM.

where we notice the refractive index modulation is proportional to the modulus square of the envelope. Due to the time-dependence of the envelope intensity, the nonlinear modulation of the refractive index will cause a time-dependent phase shift which will result in complex dynamics in the instantaneous frequency of the pulse. This effect is known as Self-Phase Modulation (SPM) and can be better explained starting from the coupled equations in the case of degenerate four-wave mixing. Following an analogous treatment to the case of second order nonlinear effect we obtain a system of four coupled equations. Imposing the degeneracy condition ($\omega_1 = \omega_2 = \omega_3 = \omega_4 = \omega_0$) it is possible to derive the so called Nonlinear Schrodinger Equation (NSE):

$$\frac{\partial A}{\partial z} - i\frac{GVD}{2}\frac{\partial^2 A}{\partial t^2} = -i\gamma|A|^2 A \tag{3.39}$$

where $\gamma = \frac{\mu_0 \omega_0 c_0 \varepsilon_0 \chi^{(3)}}{2n_0}$. In order to highlight the effect of the nonlinear term we neglect dispersion ($GVD = 0$):

$$\frac{\partial A}{\partial z} = -i\gamma|A^2|A \tag{3.40}$$

We look for solutions of the type:

$$A(z,t) = A(0,t)e^{i\varphi(z,t)} \tag{3.41}$$

Inserting the ansatz in the NSE we get:

$$A(z,t) = A(0,t)e^{-i\gamma|A(0,t)|^2 z} \tag{3.42}$$

The envelope undergoes a phase shift proportional to its intensity while the amplitude remains unchanged. Inserting the expression of the envelope in the electric field we can calculate the instantaneous frequency by taking the temporal derivative of its phase $\phi$, obtaining:

$$\omega(t) = \frac{\partial\phi}{\partial t} = \omega_0 - \gamma z \frac{\partial|A(0,t)|^2}{\partial t} \tag{3.43}$$

The phase modulation results in a different frequency shift for each part of the pulse. For $\gamma > 0$ the leading edge of the pulse experiences a red shift while the trailing edge shifts towards higher frequencies. As a consequence the pulse is symmetrically broadened with respect to the carrier frequency $\omega_0$ (see figure 3.4). The broadening associated to the time-dependent modulation of the instantaneous frequency can be exploited to generate ultrabroadband pulses. This process is called White Light Generation (WLG) and it is usually achieved with suitable crystals like sapphire, YAG or $CaF_2$.

## 3.6 Pump-Probe spectroscopy

Pump-probe spectroscopy is a powerful experimental technique used to study ultrafast carrier dynamics in a wide range of materials with femtosecond resolution. In this technique, one stronger beam (pump), resonant with a transition of choice, is used to excite the sample and is followed by a weaker pulse (probe) which monitors the pump-induced changes in the optical properties of the sample at different time delays

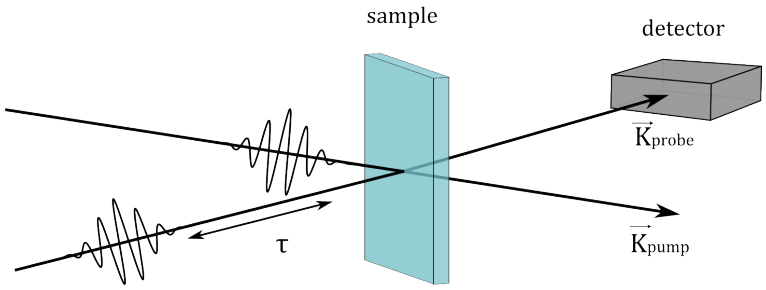


**Figure 3.5:** Non-collinear degenerate pump-probe scheme

with respect to the pump pulse arrival. By measuring these changes as a function of the time delay between the pulses it is possible to extract information about the relaxation dynamics of the electronic states in the sample. This type of experiment can be implemented in many ways depending on the characteristics of the pulses, the geometry of the setup and the measured optical properties. In this section we will consider the case of non-collinear degenerate pump-probe, illustrated in figure 3.5, in which the pulses share the same carrier frequency and propagate in different directions. Even though in practical applications the desired spectral features for the two pulses are often different, the degenerate case allows to get physical insight in the problem while simplifying calculations. In our case the quantity of interest is the relative variation of the sample reflectivity, with and without the pump, defined as:

$$\frac{\Delta R}{R} = \frac{|E_{pr}^{ON}|^2 - |E_{pr}^{OFF}|^2}{|E_{pr}^{OFF}|^2} \propto \frac{\Delta I_{pr}}{I_{pr}} \tag{3.44}$$

where $E_{pr}^{ON}$ can be expressed as the sum of the input probe field $E_{pr}^{(0)}$ and a variation $\Delta E_{pr}$ due to the coupling with the pump-induced polarization. Assuming $\Delta E_{pr} << E_{pr}^{(0)}$ we can neglect $|\Delta E_{pr}|^2$ obtaining:

$$\frac{\Delta I_{pr}}{I_{pr}} \propto \frac{2\,\mathrm{Re}\left\{E_{pr}^{(0)^*}\Delta E_{pr}\right\}}{|E_{pr}^{OFF}|^2} \tag{3.45}$$

where we have also assumed the probe to be weak enough not to perturb the sample, so that $E_{pr}^{OFF} \approx E_{pr}^{(0)}$. Upon excitation by the pump some of the electrons will be promoted from the ground state to an available excited state, thus modifying the way the sample absorbs the probe. The system will then return to its equilibrium state in an ultrafast timescale. We can model this phenomenon by considering a time-dependent perturbation of the absorption coefficient of the sample:

$$\alpha(t) = \alpha_0 + \Delta\alpha(t) \tag{3.46}$$

where $\alpha_0$ is the absorption coefficient of the unperturbed system. For a sample of thickness L, the effect of absorption can be modeled as follows:

$$E_{OUT} = E_{IN} e^{-\frac{\alpha}{2}L} \approx E_{IN} e^{-\frac{\alpha_0}{2}L}\left(1 - \frac{\Delta\alpha(t)}{2}L\right) \tag{3.47}$$

where we have assumed the perturbation to be small ($\Delta\alpha << \alpha_0$). We take as input the superposition of pump and probe fields, obtaining:

$$E_{pr}^{ON} = e^{-\frac{\alpha_0}{2}L}\left(1 - \frac{\Delta\alpha(t)}{2}L\right) \mathrm{Re}\left\{A_{pr} e^{i(\omega_0 t - \mathbf{k_{pr}}\cdot\mathbf{r})} + A_{pu} e^{i(\omega_0 t - \mathbf{k_{pu}}\cdot\mathbf{r})}\right\} \tag{3.48}$$

Considering linear regime, the perturbation can be written as the convolution between the input intensity $|E_{pr} + E_{pu}|^2$ and the causal response function of the system $h(t)$:

$$\Delta\alpha(t) = -\int_{-\infty}^{t}\left[|A_{pu}|^2 + |A_{pr}|^2 + \mathrm{Re}\left\{A_{pu}^* A_{pr} e^{i(\mathbf{k_{pu}} - \mathbf{k_{pr}})\cdot\mathbf{r}}\right\}\right] h(t - t')\, dt' \tag{3.49}$$

Considering only the field components emerging in the $\mathbf{k_{pr}}$ direction, subtracting $E_{pr}^{OFF}$ and dropping some factors for simplicity, we get:

$$\begin{aligned}\Delta E_{pr} \propto\ & \mathrm{Re}\left\{A_{pr} e^{i(\omega_0 t - \mathbf{k_{pr}}\cdot\mathbf{r})} \int_{-\infty}^{t} |A_{pu}|^2 h(t - t')\, dt'\right\} + \\ & + \mathrm{Re}\left\{A_{pu} e^{i(\omega_0 t - \mathbf{k_{pr}}\cdot\mathbf{r})} \int_{-\infty}^{t} A_{pu}^* A_{pr} h(t - t')\, dt'\right\}\end{aligned} \tag{3.50}$$

Since the detector is typically too slow to record such a fast signal, the actual quantity being measured in a real experiment is the variation in the probe transmitted energy $\Delta U_{pr}$, obtained by time integration of $\Delta I_{pr} \propto 2\,\mathrm{Re}\{E_{pr}^{(0)*}\Delta E_{pr}\}$:

$$\Delta U_{pr}(\tau) = \int_{-\infty}^{+\infty} \Delta I_{pr}(t)\,dt \propto \big[\gamma(\tau) + \beta(\tau)\big] \tag{3.51}$$

where:

$$\gamma(\tau) = \int_{-\infty}^{+\infty} |A_{pr}(t)|^2\,dt \int_{-\infty}^{t} |A_{pu}(t')|^2 h(t-t')\,dt' \tag{3.52a}$$

$$\beta(\tau) = \mathrm{Re}\left\{ \int_{-\infty}^{+\infty} A_{pu}(t)A_{pr}^*(t)\,dt \int_{-\infty}^{t} A_{pu}^*(t')A_{pr}(t')h(t-t')\,dt' \right\} \tag{3.52b}$$

We have two terms. The first one is the pump-probe signal and can be interpreted as follows: the pump saturates the absorption of the sample which is then monitored by the delayed probe pulse. The second is typically referred to as coherent artifact and is given by the coherent coupling of the pump into the probe direction. We will now focus on the first term since it is the one we are interested in. We can notice that expression (3.52a) is equivalent to:

$$\gamma(\tau) = I_{pr} \otimes [I_{pu}(t) * h(t)] \tag{3.53}$$

where $\otimes$ is the autocorrelation symbol. By applying a change of variables this can be rewritten as:

$$\gamma(\tau) = h(t) * [I_{pr}(t) \otimes I_{pu}(t)] \tag{3.54}$$

This result shows that the pump-probe signal is given by the convolution of the system response with the cross-correlation between the pump and probe pulses and explains why the temporal resolution of this technique is limited by the duration of the pulses. Indeed,

if the dynamic of the system is much shorter than the pulse duration $\big(h(t) \approx \delta(t)\big)$, then the expression simply reduces to the cross-correlation between the pulses, and no information about the system is retrieved. To obtain a complete picture of the carrier dynamics it is essential to probe the sample at different probe wavelengths, thus the measured signal will be both a function of the delay $\tau$ and the probe frequency $\omega_{pr}$:

$$\frac{\Delta R}{R}(\omega_{pr}, \tau) = \frac{R_{ON}(\omega_{pr}, \tau) - R_{OFF}(\omega_{pr})}{R_{OFF}(\omega_{pr})} \approx \Delta\alpha(\omega_{pr}, \tau) \tag{3.55}$$

The switching between $R_{ON}$ and $R_{OFF}$ is achieved by modulating the pump beam with a mechanical chopper at half the repetition frequency of the laser. In this way, each pair of consecutive probe pulses first experiences the pump-induced polarization and then the unperturbed sample. In figure 3.6 are illustrated the three different types of signal observed in a pump-probe measurement, arising from population changes inside the sample. These signals can be discriminated by the sign of $\Delta\alpha$:

- **Ground State Bleaching (GSB)**: the pump will promote carriers in the excited state reducing the population in the ground state. This will make the sample absorb less ($\Delta\alpha < 0$).
- **Excited State Absorption (ESA)**: carriers in the excited state can be further promoted to a higher energy level by the absorption of the probe ($\Delta\alpha > 0$).
- **Stimulated Emission (SE)**: the probe can induce stimulated emission from the level populated by the pump resulting in decreased absorption($\Delta\alpha < 0$). In this case, we have the same sign of GSB but SE occurs at lower energies.

As shown before, one of the requirements of a pump-probe measurement is to keep the pump-induced perturbation as small as possible.

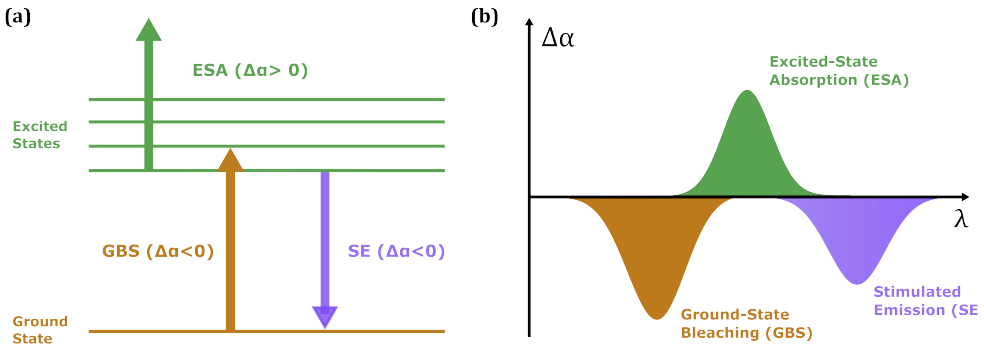


**Figure 3.6:** Different types of pump-probe signals: (a) energy level scheme of the transitions associated to the signals, (b) differential transmission spectrum.

As a consequence, these signals are usually very small and require careful preparation of the setup to be detected. In addition, they are also affected by different sources of noise such as the laser intensity noise, the shot noise of the detector and other types of electronic noises in the acquisition system. To optimize S/N, the final data are obtained by averaging different runs of the same measurement.

# Chapter 4

# Experimental setup

In this chapter we describe in detail the sample's geometrical features, optical properties and fabrication procedure (Section 1), together with the pump-probe setup employed in the experiments (Section 3). Further information regarding polarimetric measurements is provided in Section 2, aimed at explaining a polarization-sensitive detection line used in one of the experiments.

## 4.1 Sample description and fabrication

A simple schematic of the fabricated sample is shown in figure 4.1a. The sample consists of two replicas of a 4 $\times$ 7 matrix of 70 $\mu m$ $\times$ 70 $\mu m$ AlGaAs nanowires on top of a composite AlOx-GaAs substrate. Figure 4.1b shows a sketch of one of these metasurfaces while figure 4.1c illustrates the single unit cell vertical cross-section. Each of these metasurfaces implements different values of periodicity P and thickness W. In particular, the metasurface presented in this work (circled in fig. 4.1a) has geometrical parameters $P = 450$ nm and $W = 180$ nm. This configuration allows to fully exploit the band-filling effect by tuning an extended state resonance of the unperturbed sample near the bandgap of the semiconductor, which for the present case of $Al_{0.2}Ga_{0.8}As$ sits at

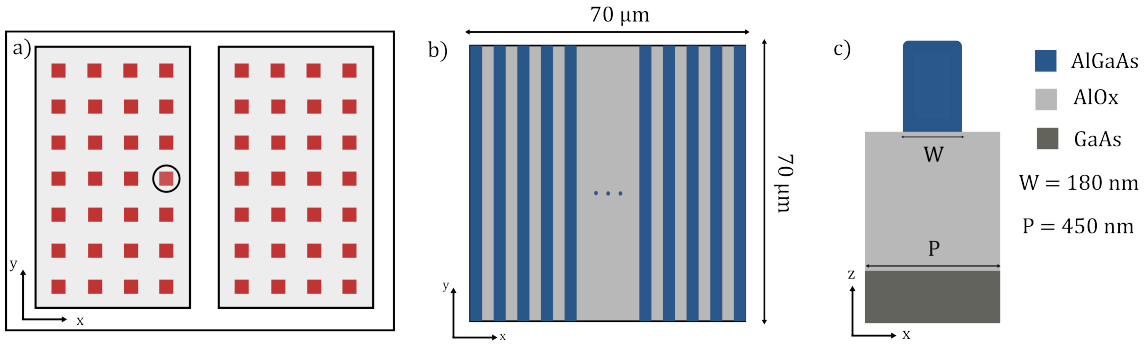


**Figure 4.1:** (a) Sketch of the fabricated sample indicating the examined metasurface. (b) Top view of the metasurface. (c) Vertical cross-section

745 nm.
The sample fabrication process is based on epitaxial growth of AlGaAs on top on AlAs wafers. This design exploits the oxidation of Aluminium Arsenide (AlAs) layer into AlOx wafers to achieve a higher optical index contrast between the AlGaAs layer ($n_{AlGaAs} \approx 3.4$) and the supporting wafer ($n_{AlOx} \approx 1.6$), which provides higher field confinement in the metaatoms. The fabrication procedure includes two steps: the desired pattern is realized through electron-beam lithography and then transferred to the substrate via reactive-ion-etching.

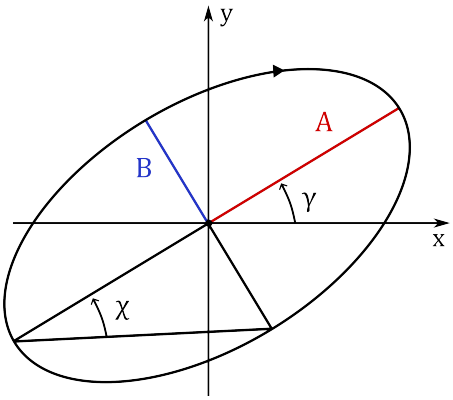


$$\begin{cases} S_0 = I \\ S_1 = I_p \cos(2\gamma)\cos(2\chi) \\ S_2 = I_p \sin(2\gamma)\cos(2\chi) \\ S_3 = I_p \sin(2\chi) \end{cases}$$

$$I_p = A^2 + B^2$$

**Figure 4.2:** Polarization ellipse and relationship of the Stokes parameters to intensity ($I$) and ellipse parameters.

## 4.2 Dynamical polarization reconstruction

The polarization state of light is usually represented through the polarization ellipse, reported in figure 4.2, which describes the line traced on the transverse plane by the tip of the electric field during propagation. A particular state of polarization is then completely determined by the 4 geometrical parameters of the ellipse (the two semiaxes, the orientation angle $\psi$ and the ellipticity angle $\chi$). However, this description poses some severe limitations in actual experiments as the quantities $\psi$ and $\chi$ are not directly measurable. An alternative description based on measurable quantities was proposed by Stokes. Considering an electromagnetic wave propagating along the $z$ axis with electric field components along x and y directions given by $E_x$ and $E_y$, respectively, and defining $I(\varphi)$ the intensity of light polarized at an angle $\varphi$ with respect to the $x$ axis, the Stokes parameters are defined as follows:

$$S_0 = I(0°) + I(90°) =< |E_x|^2 > + < |E_y|^2 > \tag{4.1a}$$
$$S_1 = I(0°) - I(90°) =< |E_x|^2 > - < |E_y|^2 > \tag{4.1b}$$
$$S_2 = I(45°) + I(135°) = \mathrm{Re}\{E_x E_y\} \tag{4.1c}$$
$$S_3 = I_{RHC} - I_{LHC} = \mathrm{Im}\{E_x E_y\} \tag{4.1d}$$

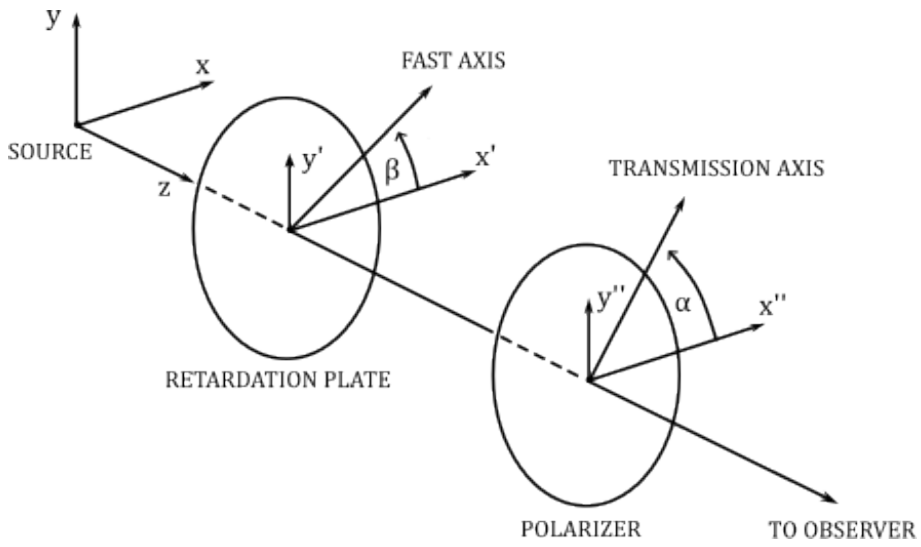


**Figure 4.3:** Schematic of the detection line used for dynamical polarization reconstruction.

where the brackets <> indicate the time average while $I_{RHC}$ and $I_{LHC}$ are the intensities of right-handed and left-handed polarized light, respectively.
In order to measure the polarization state of light we employ a system made of a retardation plate having its fast axis at an angle $\beta$ to the $x$ axis, followed by a linear polarizer with a transmission axis at an angle $\alpha$ to the $x$ axis, as shown in figure 4.3. The retardation plate introduces a phase difference $\delta$ between electric field components parallel and perpendicular to the fast axis. The reflected light intensity for an incident beam with Stokes parameters $(S_0, S_1, S_2, S_3)$ is [36]:

$$\begin{aligned} I_R(\alpha,\beta,\delta) = \frac{1}{2}\big\{ & S_0 + (S_1\cos 2\beta + S_2 \sin 2\beta)\cos 2(\alpha-\beta) \\ & + [(S_2\cos 2\beta - S_1 \sin 2\beta)\cos\delta + S_3 \sin\delta]\sin 2(\alpha-\beta)\big\} \end{aligned} \tag{4.2}$$

The Stokes parameters can be retrieved by recording the variation of $I_R(\alpha,\beta,\delta)$ as either the polarizer or the retardation plate is rotated. The rotation of the polarizer results in a rotation of the polarization plane of the transmitted light and thus the detection system must be

made insensitive to polarization by either rotating the detector together with the polarizer or by adding a depolarization element after the polarizer. For this reason, we rely on rotating the retardation plate to measure the Stokes parameters since it does not require to correct for a polarization dependent detection system. Since we are interested in characterizing the ultrafast transient behavior of the sample, we perform a pump-probe measurement recording the reflected intensity as a function of the wavelength $\lambda$ and the time delay $t$ between pump and probe pulses:

$$I_R(\lambda, t; \beta) = [r(\lambda, t; \beta) + 1] I_{OUT}(\lambda, t < 0; \beta) \tag{4.3}$$

where $r(\lambda, t; \beta) = \Delta R/R(\lambda, t; \beta)$ is the normalized transient differential reflection of the sample and $I_{OUT}(\lambda, t < 0; \beta)$ is the reflected probe intensity spectrum of the unperturbed sample. The reflected intensity $I_R(\lambda, t; \beta)$ can be expressed as a linear combination of the Stokes parameters $S_0, S_1, S_2, S_3$:

$$\begin{aligned} I_R(\lambda, t; \beta) =& c_1(\beta) S_0(\lambda, t) + c_2(\beta) S_1(\lambda, t) + \\ & c_3(\beta) S_2(\lambda, t) + c_4(\beta) S_3(\lambda, t) \end{aligned} \tag{4.4}$$

where the $c_i(\beta)$ coefficients, for the particular case of a quarter wave-plate ($\delta = \pi/2$) and linear polarizer at 45° with the x axis ($\alpha = \pi/4$), are:

$$c_1 = \frac{1}{2} \tag{4.5a}$$

$$c_2 = \frac{1}{2} \cos(2\beta) \cos(\pi/2 - 2\beta) \tag{4.5b}$$

$$c_3 = \frac{1}{2} \sin(2\beta) \cos(\pi/2 - 2\beta) \tag{4.5c}$$

$$c_4 = \frac{1}{2} \sin(\pi/2 - 2\beta) \tag{4.5d}$$

By measuring the reflected intensity for four different values of $\beta$ we can write the following linear algebraic system for each $\lambda$ and $t$:

$$\begin{bmatrix} I_R(\beta_1) \\ I_R(\beta_2) \\ I_R(\beta_3) \\ I_R(\beta_4) \end{bmatrix} = \begin{bmatrix} c_1(\beta_1) & c_2(\beta_1) & c_3(\beta_1) & c_4(\beta_1) \\ c_1(\beta_2) & c_2(\beta_2) & c_3(\beta_2) & c_4(\beta_2) \\ c_1(\beta_3) & c_2(\beta_3) & c_3(\beta_3) & c_4(\beta_3) \\ c_1(\beta_4) & c_2(\beta_4) & c_3(\beta_4) & c_4(\beta_4) \end{bmatrix} \begin{bmatrix} S_0 \\ S_1 \\ S_2 \\ S_3 \end{bmatrix} \tag{4.6}$$

from which the Stokes parameters can be retrieved.
Once the Stokes parameters are known, the ellipse parameters and the relative phase between orthogonal components can be retrieved time by time at a given wavelength according to the following formulas:

$$A = \sqrt{1/2(I_p + \sqrt{S_1^2 + S_2^2})} \tag{4.7a}$$

$$B = \sqrt{1/2(I_p - \sqrt{S_1^2 + S_2^2})} \tag{4.7b}$$

$$\gamma = 1/2 \arg(S_1 + iS_2) \tag{4.7c}$$

$$\varphi = arg[S_2 + i(-S_3)] \tag{4.7d}$$

Where $p = \sqrt{S_1^2 + S_2^2 + S_3^2}/S_0$ is the polarization fraction and $I_p = pI$ the polarized intensity. Finally, the ellipse's rotation direction can be determined by the sign of $S_3$: circulation is right-handed for $S_3 > 0$ while is left-handed for $S_3 < 0$.

## 4.3 Experimental setup

The experimental setup, reported in figure 4.4, starts from a Ti:Sapphire regeneratively amplified laser that emits 100 fs pulses centered at 800 nm with a repetition frequency of 1 kHz. The fundamental beam is separated into two branches by a beam splitter: one branch is used for generating the pump pulse while the other is used for generating the

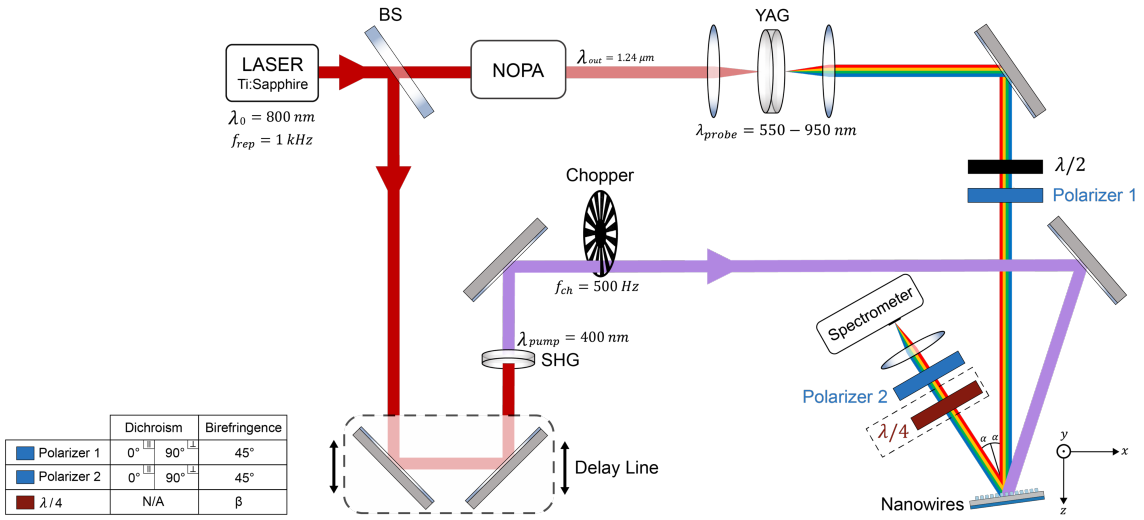


**Figure 4.4:** Synthetic sketch of the experimental setup used in the experiments. In the birefringent experiment polarizer 1 and 2 are set at 45° in the polarization plane while the quarter-wave plate is rotated at an angle $\beta$. In the dichroic experiment, polarizer 2 and quarter-wave plate are removed, whereas polarizer 1 is oriented along either the x or the z-axis.

probe pulse.
For what concerns the pump branch, the fundamental is used to pump a 1 mm Beta-Barium-Borate (BBO) crystal to generate second harmonic pulses centered at 400 nm which serve as control pulse in the experiment. In order to detect the differential signal $\Delta R/R = \frac{R'-R}{R}$ (where $R$ and $R'$ are the reflectivities of the sample with pump off and on, respectively) as a function of the pump-probe delay, an optical delay stage is inserted in the pump path. The pump beam is then modulated by a mechanical chopper at 500 Hz in order to block only half of the generated pulses. This way every 2 ms we can record the signal for both the pumped and unperturbed sample. The pump beam is then sent onto a dichroic mirror for 800 nm, set at 45°, in order to remove any residual of the fundamental, and directly focused on the sample.
Considering now the probe branch, the fundamental coming from the beam splitter is sent into a Non-collinear Optical Parametric Amplifier (NOPA) which provides amplification over a range spanning from 480

nm to 1.6 $\mu m$ with a bandwidth of 100 nm. In our case, the NOPA is tuned in order to emit pulses centered at 1240 nm which are used to pump a YAG crystal to generate a White Light Continuum (WLC) through self-phase modulation. The probe pulse obtained this way has spectrum spanning from 550 nm to 980 nm. The probe beam is then focused on the sample impinging at an angle of 9° with respect to normal incidence. In particular, the pump spot size on the sample is $260\mu m$, almost three times bigger than the probe beam diameter ($\approx 90\mu m$). This guarantees that the two pulses are always overlapped even if the control pulse is slightly shifted during the experiment.
Combining this setup with linear polarizers and waveplates allows for two types of polarization resolved pump-probe experiments, which are intended to characterize the sample in terms of ultrafast transient dichroism and ultrafast transient birefringence. As shown in figure 4.4, for the ultrafast dichroism experiment the probe beam is linearly polarized along either the x or y-axis by means of a half-wave plate followed by a suitably rotated polarizer to filter any residual unwanted polarization state. After reflection, the beam passes through a second polarizer set at the same angle of the first one. For the ultrafast birefringence measurements illumination conditions are similar to the previous case but the polarizer is now oriented at 45° in the x-y plane. After reflection, the beam is sent into a detection line comprising a quarter-wave plate oriented at an angle $\beta$ followed by a linear polarizer fixed at 45°, which allows for a time-resolved reconstruction of the Stokes parameters and the corresponding polarization ellipse, as explained in the previous section. In both experiments, the signal is recorded with a spectrometer coupled to a linear photodetector array.

# Chapter 5

# Experimental results

A full characterization of the transient anisotropic features of the sample is required to explore the different possible applications in which it can be exploited for polarization control. With this purpose, the pump-probe setup described above was used to perform two different experiments aimed at capturing the MS transient response in terms of dichroism and birefringence. The ultrafast dichroism experiment consists of measuring the differential reflection upon illumination by probe pulses having polarization state either parallel (TE mode) or perpendicular (TM mode) to the nanowires' long axis and comparing them to assess the device's efficiency in modulating its dichroic properties. This choice is justified by the particular geometry of the MS which assures the optical response to be unchanged in polarization for these modes. However, given the anisotropy of the sample, a more complex behavior is expected for mixed states of polarization feeling both dichroic axes. For this reason, in the birefringent experiment, the impinging probe was linearly polarized at 45° with respect to the nanowires. The transient modulation of the polarization ellipse was then recorded by exploiting a detection line comprising a polarizer and a quarter-wave plate, as explained in the previous chapter.
In this chapter, we report the results of such experiments and compare

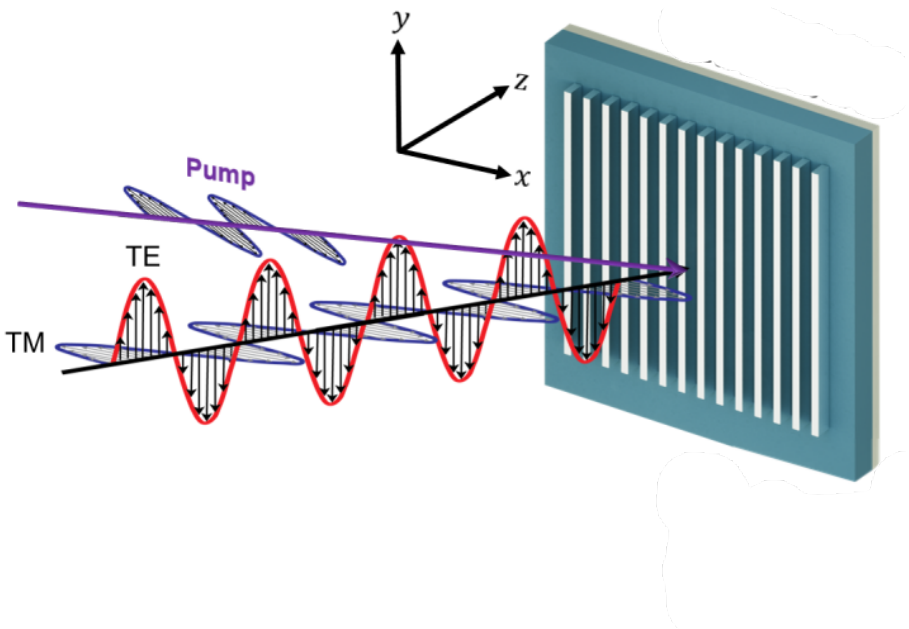


**Figure 5.1:** Sketch of the sample and illumination conditions for both static reflection measurement and pump-probe dichroic experiments.

them to the simulated values.

## 5.1 Ultrafast transient linear dichroism

A schematic of the dichroism experiment is shown in figure 5.1. The sample is excited by a pump pulse linearly polarized along the nanowire short axis and then monitored by probe pulses having either TM or TE polarization state and impinging on the sample at an incident angle of approximately 9°. We started characterizing the static response, shown in figure 5.2, by blocking the pump path and recording the reflection spectrum of the unperturbed sample for both modes. We can immediately notice that the geometric anisotropy of the sample results in a pronounced dichroic response. The TM polarization exhibits a narrow resonance at 758 nm corresponding to an extended state, which is expected since the MS was purposely designed to provide a nonlo-

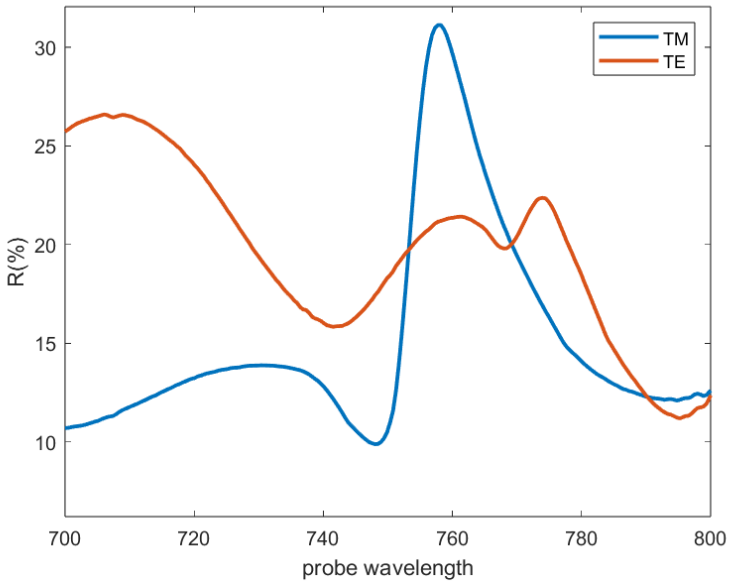


**Figure 5.2:** Static reflection response of the sample for TE (red) and TM (blue) modes as a function of the probe wavelength.

cal response, while the TE mode presents a lower asymmetric peak at longer wavelengths.
We then proceeded to characterize the photoinduced transient modulation of the MS dichroic features by performing ultrafast pump-probe experiments. The results of these measurements, reported in figure 5.3 (a-c), clearly show that the dichroic response of the sample is greatly enhanced by the optical pumping, revealing different modulations in the transient differential spectra for the two modes. For the TM case, we observe a huge signal (up to 470% which is 5 times higher than in previous investigations) in a narrow spectral range centered around 750 nm. Such remarkably high signals can arise as artifacts of the chosen figure of merit $\Delta R/R$ in spectral regions where the static reflection is infinitesimal. However, the static reflectivity at 750 nm is approximately 10%, so we can claim that this result is a real feature of the MS. On the other hand, the TE maps show narrow and broadband

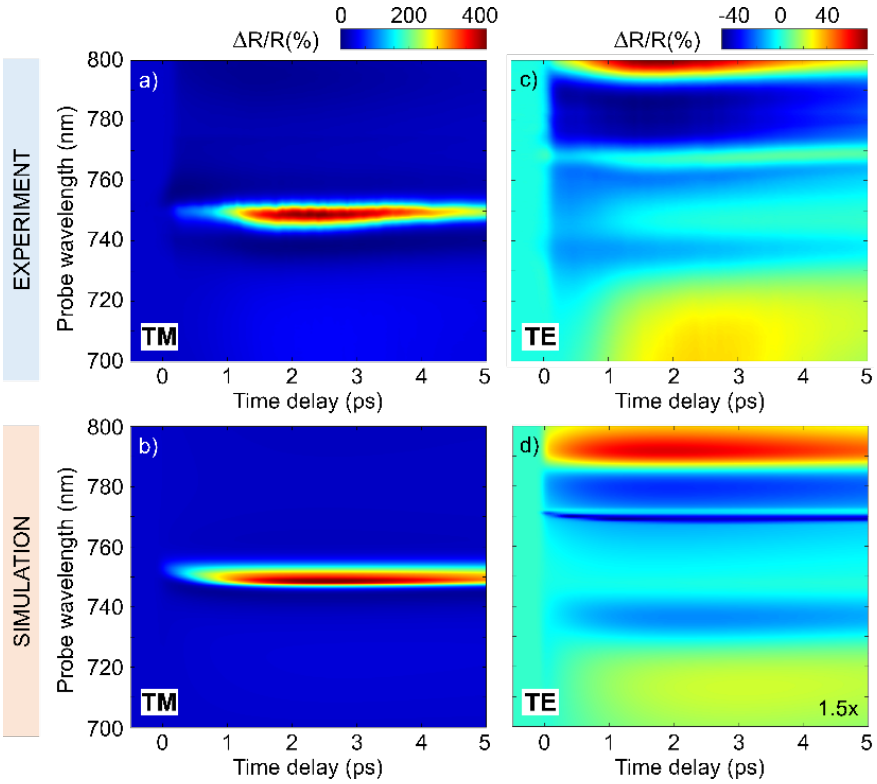


**Figure 5.3:** (a-b) Experimental and simulated TM differential reflection (expressed as a percentage) as a function of wavelength and time delay. (c-d) Same for TE polarization.

features with much lower modulations of the reflectivity with relatively low value (10%) at 750 nm and reaching a peak of 70% around 800 nm. Moreover, the transient response is extinguished in both cases in less than 15 ps, a crucial aspect in the development of a device capable of ultrafast modulation of its optical properties. It is important to note that these results were achieved under a pump fluence $F = 70\mu J/cm^2$ which is more than an order of magnitude below the damage threshold for AlGaAs, leaving space for improvement.
A closer inspection of the spectral and temporal cross-sections of the pump-probe maps further highlights these features. Figure 5.4a shows temporal dynamics for specific wavelengths. The maximum peak is observed at 2 ps with a significant delay compared to the pump pulse duration. From figure 5.4c we can see that at this specific time delay the TE modulation is almost negligible compared to the TM case.
These results can be interpreted by applying a multistep semiclassical

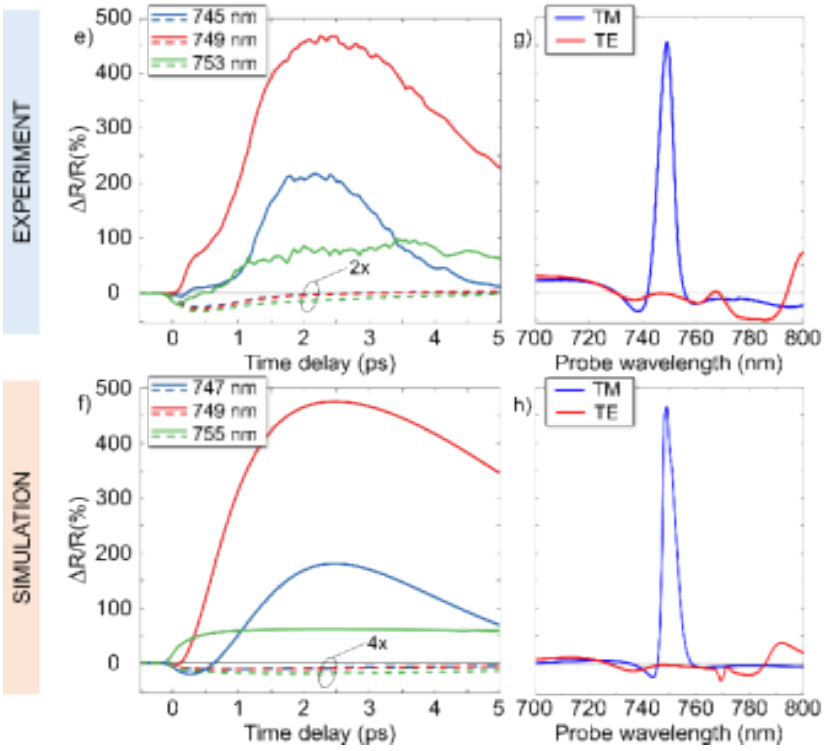


**Figure 5.4:** (a-b) Experimental and simulated temporal cross-sections, taken at wavelengths specified in the legend, for both TE and TM modes. (c-d) TE and TM spectral cross-sections at 2 ps.

modeling approach. The sample is excited by the pump pulse via linear absorption resulting in the generation of electron-hole pairs which are mostly concentrated in hotspots near the nanowires' surface since their thickness ($W = 400nm$) is much larger than the skin depth of AlGaAs ($\approx 16nm$). Following photoexcitation, this out-of-equilibrium population of carriers diffuses in a few picoseconds towards the bulk region of the wires where nonradiative carrier relaxation takes place. This process is mostly mediated by trap-assisted recombination, enabled by the presence of surface defect states, due to the large surface-to-volume ratio which makes it predominant over Auger recombination typical of bulk materials. Finally, complete equilibration of the carrier distribution occurs in tens of picoseconds through electron-phonon scattering with a consequent increase in the lattice temperature. The carrier dynamics can be then described by a simple rate equation system (Three-Temperature Model, TTM) taking into account the time evolution of

these degrees of freedom (the carrier density in the hotspots near the surface, the carrier density in the bulk region and the lattice temperature) each of which contributes to a transient modulation of the sample permittivity. In particular, the permittivity variation associated with the electron-hole pair evolution is driven by two mechanisms. The first is a typical Drude process for intraband transitions. The second is the so-called band-filling effect arising from the saturation of absorption channels: the probe finds the lower part of the conduction band already filled by the pump absorption and thus interband transitions are prohibited by Pauli exclusion principle. This results in a negative contribution to the variation of the imaginary permittivity, which directly translates into a modification of the real part due to Kramers-Kronig relations. More importantly, the probe, having energy below the bandgap, experiences a permittivity modulation that is purely real. Therefore, losses are minimized near the bandgap where band-filling dominates. The last contribution is given by the lattice heating via thermo-optical effect. The computed permittivity can then be used to retrieve the optical response by performing full-wave electromagnetic simulations. Simulated values displayed in figures 5.3 (b-d) and 5.4 (b-d) are in excellent agreement with the experimental results for both states of polarization. Since the model is able to capture the transient dynamics with such accuracy, it is interesting to use it to investigate the physical mechanism responsible for this specific TM response. Figure 5.5a compares reflectivity for the unperturbed and perturbed cases, the latter obtained from the differential signal by applying the simple formula $R'(t) = [\Delta R/R]_{measured}(t) \cdot R + R$, where R is the static reflection. We can see that the static resonance experiences a blueshift, occurring already after 850 fs from photoexcitation, and is sitting at 748 nm in correspondence with the 470% peak previously encountered at 2 ps. The same evolution is observed in the simulations reported in figure 5.5b. It is useful to plot the different contributions to the

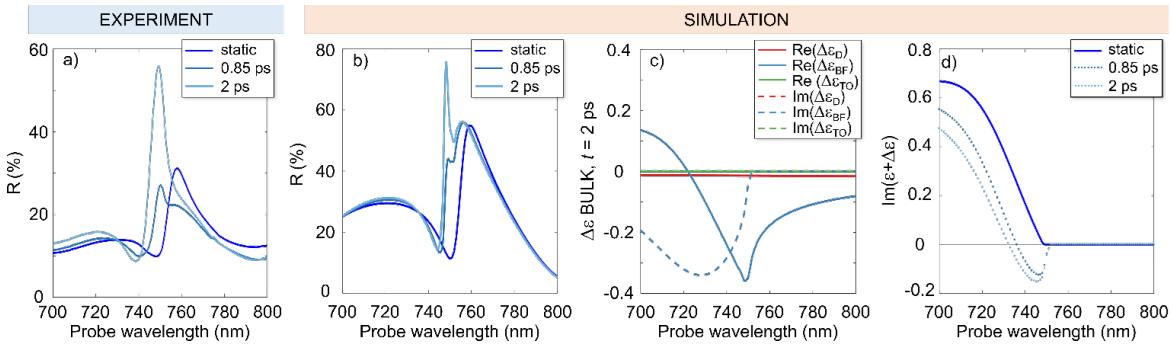


**Figure 5.5:** (a) TM reflection measured in static conditions, at 0.85 ps and at 2ps after pump arrival. (b) Simulated values for the same three cases. (c) Contributions to the real (solid lines) and imaginary (dashed lines) parts of the permittivity variation for Drude (red), band filling (blue) and thermo-optics effects (green). (d) Imaginary part of the total permittivity before and after pump arrival.

permittivity variation to disentangle the effects of the physical mechanisms involved. The results are reported in figure 5.5c. It can be seen that the lattice contribution is negligible since it becomes significant at longer timescales than the carrier lifetime. More interestingly, a comparison between Drude and band-filling contributions confirms that the relevant features of the optical response emerge from this last mechanism. Note that the total contribution to the real part of $\Delta\varepsilon$ has a negative sign, corresponding to the blueshift observed in the experiments, whereas the imaginary part exhibits a negative variation up to 750 nm, consistent with the saturation of absorption channels. Since the resonant peak is located at 748 nm where absorption is still present, it is essential to examine the imaginary part of the total transient permittivity $\varepsilon'(t) = \varepsilon + \Delta\varepsilon(t)$, where $\varepsilon$ is the unperturbed value. As can be seen from figure 5.5d, in the first picosecond after pump arrival, the total permittivity experiences a negative modulation in a narrow spectral range comprised between 738 and 750 nm. This corresponds to the opening of an optical gain window exactly in the spectral region

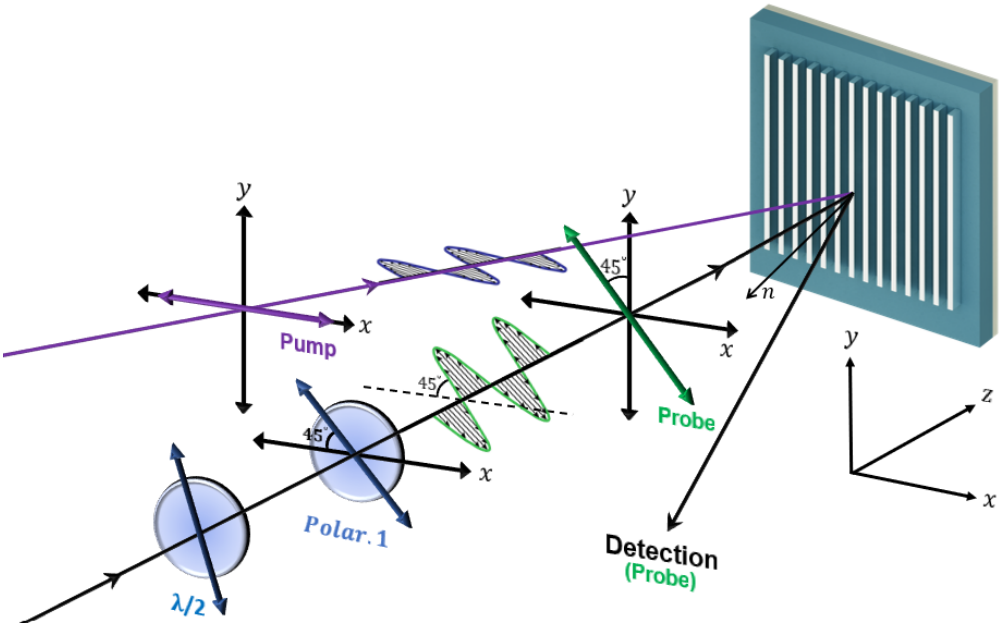


**Figure 5.6:** Illumination scheme for the birefringent experiment.

of the perturbed TM resonant mode, which reaches its maximum after 2 ps. The efficient increase in reflection can then be understood as an interplay between stimulated emission, triggered by the probe and caused by a pump-induced population inversion, and the shift of the TM resonance towards this spectral region.

## 5.2 Ultrafast transient birefringence

Excitation and detection schemes for the birefringent experiment are reported in figures 5.6 and 5.7, respectively. Photoexcitation is produced by a TM polarized control pulse and the transient response is monitored by a probe pulse linearly polarized at 45° with respect to the nanowires. After reflection, the probe passes through a detection line consisting of a quarter-wave plate, oriented at a certain angle $\beta$, followed by a linear polarizer rotated at 45°. As explained in the previous chapter, the transient modulation of the polarization ellipse can be

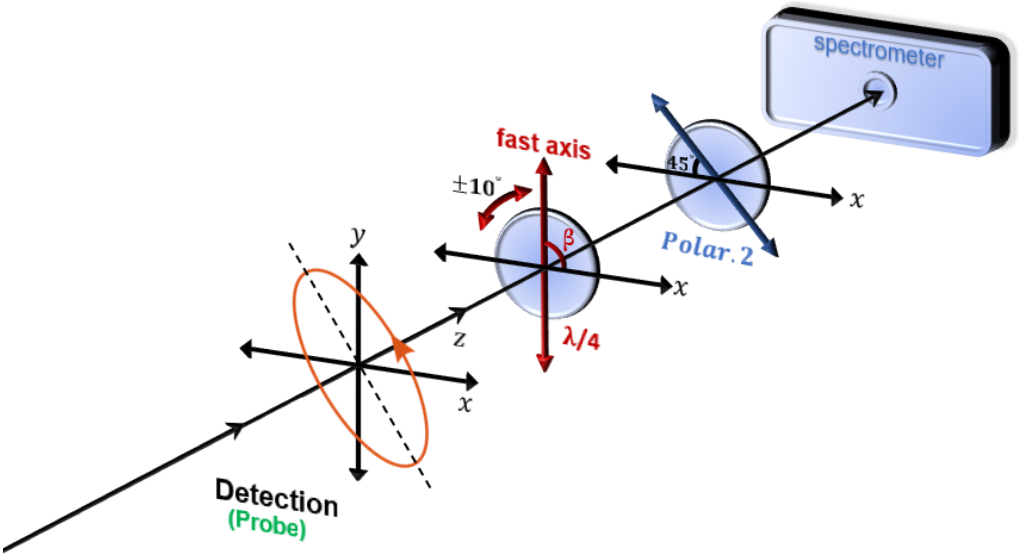


**Figure 5.7:** Sketch of the detection line used in the birefringent experiment.

then reconstructed at each wavelength and time delay by recording differential reflection maps for different orientations of the $\lambda/4$ retarder. In particular, we recorded the reflected spectrum for 15 different angles with 10° steps. Even though only 4 beta values are needed to fully reconstruct the Stokes parameters, this redundancy allows us to perform calculations on 3 different sets of angles thus guaranteeing the consistency of our measurements.
The results of this experiment are reported in figure 5.8, showcasing differential pump-probe maps for selected angles. In this case, we can notice both narrow and broad spectral features resembling a superposition of the TE and TM maps obtained in the dichroism measurements. This is consistent with the fact that the probe is now linearly polarized at 45° with respect to the nanowires and thus can excite states along the two axes of the metasurface. More importantly, the maps show significantly distinct features which is a crucial part in the reconstruction

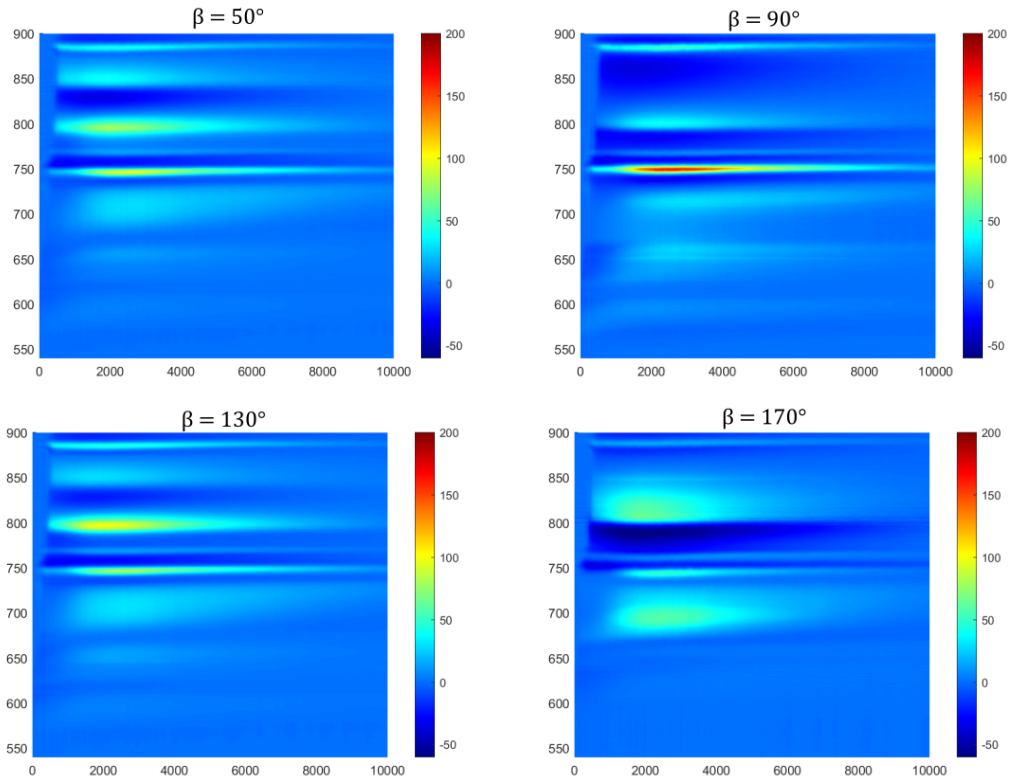


**Figure 5.8:** Differential reflectivity as a function of wavelength and time delay for selected $\beta$ values (50°, 90°, 130°, 170°).

of the polarization state based on a set of independent measurements. Once the reflected intensity spectra are recorded, we can finally retrieve the Stokes parameters from which the relative phase between TE and TM modes can be computed and the polarization ellipse reconstructed. This problem was formalized by applying Jones calculus: the Jones vector for the incident wave can be written as a superposition of TE and TM modes, while the reflected beam is expressed in terms of reflected amplitudes $(\rho_{TM}, \rho_{TE})$ and phases $(\varphi_{TM}, \varphi_{TE})$. In particular, we chose the relative phase $\varphi = \varphi_{TM} - \varphi_{TE}$ as a figure of merit of the transient response to verify if the sample can be exploited as a retarder. The results, reported in figure 5.9, show that also in this case the relevant features are located in the spectral interval 740-750 nm, suggesting that the physical mechanism is the same of the dichroic response. However, a variation in the polarization state entails a modification of both the amplitude and relative phase of the two components, resulting in much more complex dynamics. In figure

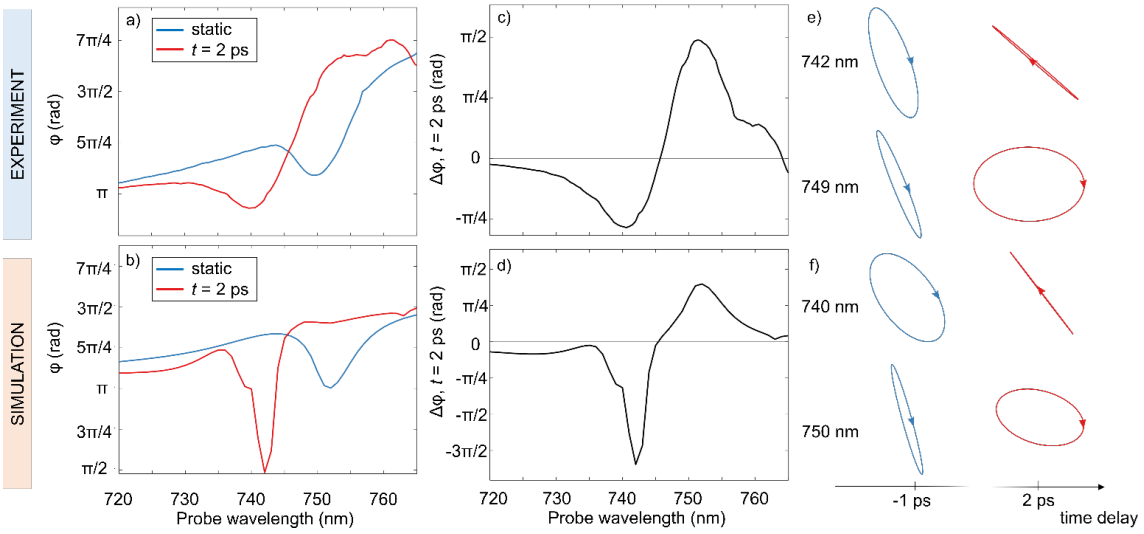


**Figure 5.9:** (a-b) Comparison between phases in static ($\varphi$) and perturbed ($\varphi'$) conditions at 2 ps, for both experimental and simulated results. (c-d) Experimental and simulated transient relative phase shift between components at 2 ps. (e-f) Reconstructed polarization ellipse in static (-1 ps) and perturbed (2ps) conditions from experimental and simulated values.

5.9 (a-b) phases for the static ($\varphi$) and perturbed response at 2 ps ($\varphi'$) are compared, while figure 5.9 (c-d) displays the transient variation $\Delta\varphi = \varphi' - \varphi$. At 749 nm, after photoexcitation, the sample introduces an additional $\pi/2$ relative phase shift between orthogonal components and thus acts like a transient quarter-wave plate. In other words, if the static response is linearly polarized, perturbation results in an ultrafast linear-to-circular polarization conversion. This result is confirmed by the evolution of the reconstructed polarization ellipse, reported in figure 5.9 (e-f).

# Chapter 6

# Conclusions

We have presented an all-dielectric metasurface working in reflection for the control of polarization, together with a customized pump-probe setup for ultrafast polarization analysis. The setup was used to perform two different pump-probe experiments aimed at characterizing the transient anisotropic features of the sample in terms of dichroism and birefringence. The metasurface is based on a subwavelength array of AlGaAs nanowires supported by an Al-Ox buffer on top of a GaAs substrate. This configuration is capable of very efficient all-optical modulation of dichroism and birefringence, enabled by the interplay between the tuning of a high-quality factor extended state near the bandgap of the semiconductor and the photoinduced band-filling effect. In particular, our results show outstanding modulations of the dichroic response for TM polarized light, with a peak of 470%, and remarkable phase modulations up to $\pi/2$ in the spectral region near the bandgap, confirming the origin of the response. These results thus portray the examined metasurface as a promising compact and ultrafast alternative to conventional polarization optics. Moreover, this design can be easily extended to other wavelength operating regimes by tuning the spectral position of the bandgap varying the percentage of Al. Lastly, the efficiency of the device can be improved by exploiting the

band-filling effect in synergy with resonances having a much higher quality factor

# Bibliography


[1] E. Yablonovitch, "Inhibited spontaneous emission in solid-state physics and electronics," Phys. Rev. Lett. 58, 2059–2062 (1987)

[2] J. B. Pendry, "Negative refraction makes a perfect lens," Phys. Rev. Lett. 85, 3966–3969 (2000).

[3] Veselago, V. G., The electrodynamics of substances with simultaneously negative values of $\epsilon$ and $\mu$, Sov. Phys. Usp. 10: 509 (1968).

[4] J. Pendry, A. Holden, D. Robbins, and W. Stewart, "Magnetism from conductors and enhanced nonlinear phenomena," IEEE Trans. Microw. Theo. and Techn. 47, 2075–2084 (1999).

[5] J. B. Pendry, A. J. Holden, W. J. Stewart, and I. Youngs, "Extremely low frequency plasmons in metallic mesostructures," Phys. Rev. Lett. 76, 4773–4776 (1996).

[6] Maier, S.A. Plasmonics: Fundamentals and Applications; Springer Science & BusinessMedia: Berlin, Germany, 2007.

[7] Khurgin JB. How to deal with the loss in plasmonics and metamaterials. Nat Nanotechnol 2015; 10: 2–6.

[8] Arseniy I. Kuznetsov et al. , Optically resonant dielectric nanostructures. Science354,aag2472(2016).

[9] Alexander Krasnok, Sergey Makarov, Mikhail Petrov, Roman Savelev, Pavel Belov, and Yuri Kivshar "Towards all-dielectric metamaterials and nanophotonics", Proc. SPIE 9502, Metamaterials X, 950203 (5 May 2015); https://doi.org/10.1117/12.2176880

[10] Baranov DG, Zuev DA and Lepeshov SI et al. All-dielectric nanophotonics: the quest for better materials and fabrication techniques. Optica 2017; 4: 814–25.

[11] C. F. Bohren, D. R. Huffman, Absorption and Scattering of Light by Small Particles (Wiley, 1983).

[12] Tzarouchis, D.; Sihvola, A. Light Scattering by a Dielectric Sphere: Perspectives on the Mie Resonances. Appl. Sci. 2018, 8, 184.

[13] Schirato, Andrea, Maiuri, Margherita, Cerullo, Giulio and Della Valle, Giuseppe. "Ultrafast hot electron dynamics in plasmonic nanostructures: experiments, modelling, design" Nanophotonics, vol. 12, no. 1, 2023, pp. 1-28. https://doi.org/10.1515/nanoph-2022-0592

[14] C. F. Bohren, "How can a particle absorb more than the light incident on it?" American Journal of Physics, vol. 51, pp. 323-327, 1983

[15] V. Giannini, A. I. Fernández-Domínguez, S. C. Heck, and S. A. Maier, "Plasmonic nanoantennas: fundamentals and their use in controlling the radiative properties of nanoemitters," Chem. Rev., vol. 111, pp. 3888-3912, 2011.

[16] X. Li, D. Xiao, and Z. Zhang, "Landau damping of quantum plasmons in metal nanostructures," New J. Phys., vol. 15, p. 023011, 2013.

[17] Kazuo Watanabe, Dietrich Menzel, Niklas Nilius, and Hans-Joachim Freund, "Photochemistry on Metal Nanoparticles", Chemical Reviews 2006 106 (10), 4301-4320 DOI: 10.1021/cr050167g

[18] Kuznetsov, A. I., Miroshnichenko, A. E., Fu, Y. H., Zhang, J., and Luk'yanchuk, B., "Magnetic light," Sci. Rep. 2, 1 (2012).

[19] P. Y. Yu and M. Cardona, Fundamentals of Semiconductors (Springer, 2010).

[20] M. Kerker, D. Wang, G. Giles, Electromagnetic scattering by magnetic spheres. J. Opt. Soc. Am. 73, 765–767 (1983). doi: 10.1364/JOSA.73.000765

[21] Balanis, Constantine A. (2015). Antenna Theory: Analysis and Design, 4th Ed. John Wiley & Sons. pp. 302–303. ISBN 978-1119178989.

[22] Bharadwaj, P., Deutsch, B. & Novotny, L. Optical antennas. Adv. Opt. Photon. 1, 438–483 (2009).

[23] Yu N, Genevet P, Kats M A, Aieta F, Tetienne J-P, Capasso F and Gaburro Z 2011 Light propagation with phase discontinuities: generalized laws of reflection and refraction Science 334 333–7

[24] Simovski, C., & Tretyakov, S. (2020). An Introduction to Metamaterials and Nanophotonics. Cambridge: Cambridge University Press.

[25] Karim Achouri, Christophe Caloz (2021). Electromagnetic Metasurfaces: Theory and Applications. Wiley-IEEE Press

[26] Fei Ding et al 2018 Rep. Prog. Phys. 81 026401

[27] Treatise on Light. By Christiaan Huygens. Rendered into English by Silvanus P. Thompson. London, Macmillan & Company. 1912. Pp. vii +128.

[28] Pierre Berini, "Optical Beam Steering Using Tunable Metasurfaces" ACS Photonics 2022 9 (7), 2204-2218 DOI: 10.1021/acsphotonics.2c00439

[29] Nemati A, Wang Q, Hong M H, Teng J H. Tunable and reconfigurable metasurfaces and metadevices. Opto-Electron Adv 1, 180009 (2018). doi: 10.29026/oea.2018.180009

[30] Shcherbakov, M.R., Liu, S., Zubyuk, V.V. et al. Ultrafast all-optical tuning of direct-gap semiconductor metasurfaces. Nat Commun 8, 17 (2017). https://doi.org/10.1038/s41467-017-00019-3

[31] He, Y., Song, B. & Tang, J. Optical metalenses: fundamentals, dispersion manipulation, and applications. Front. Optoelectron. 15, 24 (2022). https://doi.org/10.1007/s12200-022-00017-4

[32] Ding, F., Tang, S. and Bozhevolnyi, S.I. (2021), Recent Advances in Polarization-Encoded Optical Metasurfaces. Adv. Photonics Res., 2: 2000173. https://doi.org/10.1002/adpr.202000173

[33] Qian C, Zheng B, Shen Y, Jing L, Li E, Shen L, et al. Deep-learning-enabled self-adaptive microwave cloak without human intervention. Nat Photon. (2020) 14(6):383–90. doi:10.1038/s41566-020-0604-2

[34] Della Valle, G., Hopkins, B., Ganzer, L., Stoll, T., Rahmani, M., Longhi, S., Kivshar, Y. S., Angelis, C. D., Neshev, D. N., and Cerullo, G. (2017). Nonlinear anisotropic dielectric metasurfaces for ultrafast nanophotonics. ACS Photonics, 4(9):2129–2136.

[35] Andrew M.Weiner. Ultrafast Optics. 1st ed. Wiley, 2009. isbn: 9780471415398

[36] H. G. Berry, G. Gabrielse, and A. E. Livingston, "Measurement of the Stokes parameters of light," Appl. Opt. 16, 3200-3205 (1977)